Spatial Asymmetries of the Prophase Nucleus Regulate Dynein Recruitment to Ensure Mitotic Fidelity

Vanessa Nunes[1,2,3], Margarida Dantas[1,2,3], Elisa Vitiello[4], Irene Wang[4], Nicolas Carpi[5,6], Martial Balland[4], Matthieu Piel[5,6], Paulo Aguiar[1,7], Helder Maiato[1,2,8], Jorge G. Ferreira[1,2,8,9]

1 - Chromosome Instability & Dynamics Lab, Instituto de Investigação e Inovação em Saúde (i3S), Porto, Portugal; 2 – Instituto de Biologia Celular e Molecular (IBMC), Porto, Portugal; 3 – BiotechHealth PhD program, Instituto de Ciências Biomédicas (ICBAS), Porto, Portugal; 4 –Laboratoire interdisciplinaire de Physique, Université Joseph Fourier (Grenoble 1), France; 5 - Institut Curie, PSL Research University, CNRS, UMR 144, F-75005 Paris, France; 6 – Institut Pierre-Gilles de Gennes, PSL Research University, F-75005 Paris, France; 7 – Instituto Nacional de Engenharia Biomédica (INEB), Porto, Portugal; 8 – Departamento de Biomedicina, Faculdade de Medicina do Porto, Portugal.
9 - Lead contact

Corresponding author: Jorge G. Ferreira (jferreir@ibmc.up.pt)

Summary:

Accurate chromosome segregation during mitosis requires the efficient assembly of a microtubule-based structure known as the mitotic spindle. To achieve this, most cells rely on centrosomes, which must separate to establish a bipolar configuration. Several molecular components are involved in centrosome movement but how their activities are coordinated in space and time remains unknown. Here, we provide an integrated mechanistic view that explains how cell geometry influences centrosome positioning and investigate the respective consequences for spindle assembly and mitotic fidelity. We demonstrate that the initial axis of centrosome separation depends on cytoskeletal tension and cortical Dynein distribution. As mitotic cells round up and tension decreases, the centrosomes and nucleus reorient so that centrosomes are positioned on the short nuclear axis during nuclear envelope breakdown (NEB). We demonstrate how mitotic chromosome condensation creates a stiffness asymmetry on the prophase nucleus to enable polarized Dynein loading on the nuclear envelope (NE), thus ensuring correct centrosome positioning. We further show that Dynein polarization, but not loading, depends on an intact microtubule network and nuclear lamina. Finally, we show that centrosome positioning on the short nuclear axis is relevant for the fidelity of chromosome segregation. These results demonstrate how Dynein recruitment is mechanically regulated to ensure accurate chromosome segregation.

Introduction:

In order to properly segregate chromosomes, cells need to assemble a bipolar spindle. Although multiple pathways contribute to spindle assembly (Prosser and Pelletier, 2017), in human somatic cells this process relies mainly on centrosomes, the main microtubule (MT)-organizing centers. In preparation for mitosis, duplicated centrosomes need to separate along the nuclear envelope. Forces required to separate centrosomes are generated by the action of kinesin-5, which slides anti-parallel MTs apart (Whitehead et al., 1996). Accordingly, depletion or inhibition of kinesin-5 prevents centrosome separation, leading to the formation of monopolar spindles and a mitotic arrest (Kapoor et al., 2000). In addition, other players have been involved in the process, which include

Dynein, as well as actin, myosin II and MTs (Tanenbaum and Medema, 2010). However, how these different components are functionally coordinated remains unclear. More specifically, we do not know how the force generated by these different players can be directed in such a way to migrate centrosomes to opposite sides of the nucleus.

Centrosome separation was previously described to occur independently of nuclear envelope breakdown (NEB) (Rattner and Berns, 1976). As a consequence, two pathways for spindle assembly were proposed: in the Prophase pathway ("P pathway"), cells separate their centrosomes prior to NEB, whereas in the Prometaphase pathway ("PM pathway"), centrosomes separate only after NEB (Kaseda et al., 2012; Silkworth et al., 2012; Whitehead et al., 1996). While compelling, these data were obtained from cells seeded on non-physiological substrates such as uncoated coverslips and thus, overlook the contributions of cellular shape and extracellular cues for the process. These limitations might also explain why some reports describe the two pathways occurring with equivalent frequency (Kaseda et al., 2012; Whitehead et al., 1996), whereas others show a clear bias towards the P pathway (Mardin et al., 2013). Therefore, clarifying this issue is extremely relevant, as centrosome positioning can affect mitotic fidelity on multiple levels (Kaseda et al., 2012; Mardin et al., 2013; Silkworth et al., 2012).

During mitotic entry, the cytoskeleton reorganizes to form a stiff mitotic cortex (Kunda et al., 2008) that facilitates bipolar spindle assembly (Lancaster et al., 2013). This requires disassembly of interphase adhesion complexes (Dao et al., 2009; Marchesi et al., 2014), retraction of cell margins (Cramer and Mitchison, 1997) and changes in MT dynamic cytoskeleton (Zhai et al., 1996). Importantly, these cytoskeletal events should be synchronized with nuclear events such as MT-dependent tearing of the nuclear envelope (NE) (Beaudouin et al., 2002; Salina et al., 2002) and Lamin A removal from the nuclear lamina (Georgatos et al., 1997), to ensure coordination between NEB and mitotic spindle assembly. However, the mechanistic link between cytoplasmic and nuclear events remains to be determined.

In this study, we performed a high-resolution live cell imaging analysis of centrosome behavior mitotic entry, followed by cellular reconstruction. Our data show that cytoskeletal tension determines the initial centrosome separation axis, through the action of cortical Dynein. Subsequent mitotic cell rounding reorganizes the cytoskeleton, displacing cortical Dynein, decreasing tension and releasing centrosomes from the traction axis. This allows centrosomes to be positioned on the short nuclear axis at NEB, in a process that depends on the mechanical properties of the nucleus. As a result, bipolar spindle assembly is facilitated, ensuring maximum exposure of kinetochores to MTs, which facilitates chromosome capture and improves chromosome segregation fidelity.

Results:

Extracellular cues are important for spindle assembly

To better characterize centrosome positioning and spindle assembly we performed high spatial and temporal resolution live-cell imaging. Our results show that HeLa cells seeded on a non-physiological substrate (poly-L-lysine; PLL) can follow either pathway of centrosome separation (Fig. S1A), as reported previously. However, when seeded on fibronectin (FBN), approximately 82% of the cells separate their centrosomes to opposite sides of the cell before NEB, thus following the "P pathway". In addition, cells that have

an increased spreading area at NEB show longer pole-to-pole distances (Fig. S1B), suggesting that centrosome separation prior to NEB is a function of the cell adhesion area. To normalize cell area and shape conditions, we seeded cells on defined FBN micropatterns that allowed precise geometrical confinements. We used HeLa cells stably expressing EB3-GFP (MT tip marker) and Lifeact-mCherry (actin marker) to monitor centrosome dynamics, cell membrane and nuclear shape. We started by observing centrosomes, cell membrane shape and nucleus in lines with 10μm width (Fig. 1). Subsequent reconstruction of centrosome trajectories, cell and nuclear membranes was performed to extract quantitative data from the datasets (Fig. S2). Under these conditions, approximately 90% of the cells separated centrosomes to opposite sides of the nucleus before NEB. Centrosome dynamics relative to the underlying micropattern was analyzed by defining two angles theta and phi, which reflect movements in xy and z, respectively, and vary between 0º (aligned with pattern) and 90º (perpendicular to the pattern). Our data shows that theta and phi have lower values at early (~800 sec before NEB) and later stages (~600 sec after NEB), but increase near NEB (Fig. 1B). This deviation from the pattern occurred simultaneously with mitotic cell rounding, as measured by the decrease in cell membrane eccentricity (Fig. 1C and S3). This suggests that centrosome movement could be coupled with cell rounding, prompting us to analyze the later event with higher detail. Given that cells were seeded on line patterns, we defined two regions of rounding, corresponding to the tips of the elongated cell (Fig. 1D, 0º). Cell rounding began ~800 sec before NEB, with 80% of the cells showing asymmetric rounding (Fig. 1C-E). Significant differences in membrane retraction velocity were also observed (mean velocity of 2.8μm/min for side 1 and 1.1 μm/min for side 2, arbitrarily defined; Fig. 1F). Reorganization of the cell cortex at the tips of the elongated cell occurred with a simultaneous thinning and expansion of the lateral cortex (Fig. 1D, 90º; Fig. 1G), with average cortical width changing from 14.7μm to 16.2 μm. We conclude that centrosomes deviate from the underlying micropattern simultaneously with an extensive cytoskeletal reorganization.

Metaphase spindle orientation is determined by the distribution of actin-based retraction fibers and this depends on extracellular matrix organization (Fink et al., 2011; Mitchison, 1992; Thery et al., 2005). While our results confirmed that centrosomes align with the pattern at later stages, the observed deviation centrosomes showed as cells rounded up (Fig. S3), suggests they transiently ignore extracellular cues closer to NEB. Interestingly, we observed that during this period centrosomes tend to move along the nuclear envelope so that, upon NEB, they are positioned on the short nuclear axis (approximately 80% of cells; Fig. 1H and I). This behavior depended mainly on initial spreading area but not on cell shape (Fig. 2 and Fig. S4), as changing from a polarized shape such as a rectangles to an unpolarized large circle did not block the capacity of centrosomes to position on the short nuclear axis (78% of cells on rectangles and 75% of cells on large circles; Fig. 2A, B, D, E and S4). However, when cells were placed in small circles, centrosome movement became erratic and they were no longer able to find the short nuclear axis (Fig. 2C, F and S4). Under these conditions, only 25% of cells were able to position centrosomes on the short nuclear axis. Overall, these data indicate that cell area is required for centrosome positioning on the short nuclear axis.

Cytoskeletal tension defines the initial centrosome separation axis

Centrosomes only moved towards the short nuclear axis when mitotic cells rounded up. This suggests that cytoskeletal tension might block this process by exerting pulling forces

on centrosomes. To clarify this, we first performed Traction Force Microscopy (TFM) analysis to determine whether the initial axis of centrosome separation is aligned with the traction force axis defined by the micropattern. Indeed, when seeded on rectangular micropatterns, cells present a well-defined traction axis orientation which correlated with the initial centrosome separation axis (theta; Fig. 3A-C). During mitotic rounding, both cell area and contractile energy, as measured by TFM, decreased (Fig. 3D), supporting our initial hypothesis that rounding releases centrosomes from the tensional forces. Interestingly, when cells were seeded on circles, although there was no preferred traction axis orientation, centrosomes still oriented according to the underlying traction axis (Fig. S5). This is consistent with our previous observation that cells on large circles were still able to position centrosomes correctly, even though they had no obvious long cell axis (Fig. 2A, B). Similarly to what we observed for cells on rectangles, the decrease in cell area correlated with a concomitant decrease in the contractile energy (Fig. S5D). Taken together with our previous observations, these results strongly suggest that traction forces exerted by the cell orient the centrosomes and, once mitotic rounding begins, the decrease in forces allows centrosomes to be released and move towards the short nuclear axis. To further test this hypothesis, we decided to interfere with cytoskeletal tension. To do this, we expressed a constitutively active mutant form of the small GTPase Rap1 (Rap1Q63E; hereafter referred to as Rap1*), which is known to inhibit adhesion disassembly during mitotic entry (Dao et al., 2009) and increases cytoskeletal tension (Freeman et al., 2017). Accordingly, we observed that Rap1* expression significantly delayed mitotic cell rounding and centrosome movement (Fig. 3E-G and Fig. S6A and B), which prevented centrosome positioning on the short nuclear axis (Fig. 3H). Inversely, decreasing tension by treating cells with the Rho kinase (ROCK) inhibitor Y-27632 led to premature centrosome movement as seen by the increase in theta and phi between -800sec and -200sec prior to NEB, when compared to controls (Fig. 3E-G). Interestingly, this did not compromise positioning on the short nuclear axis, as the increase in theta and phi reflected centrosome movement towards the short nuclear axis (Fig. 3H). Similar results were obtained using the MyosinII inhibitor para-Nitro-blebbistatin (our unpublished observations). Overall, these results demonstrate that cytoskeletal tension is required to maintain initial alignment of the centrosomes with the underlying extracellular matrix, which is consistent with the existence of cortical force generators that pull on astral microtubules to move centrosomes in early mitosis (Cytrynbaum et al., 2003; Sommi et al., 2011).

Given that cortical Dynein is the main molecular motor generating pulling forces on microtubules to move asters (Laan et al., 2012), we anticipated that cortical Dynein may be polarized according to the underlying micropattern. To test this, we imaged cells expressing Dynein light chain LC8 tagged with GFP. Accordingly, LC8 localized to small puncta near the substrate that were concentrated on the tips of the elongated cells as well as centrosomes (Fig. 3I). Interestingly, cortical LC8 localization was lost as cells started rounding, which correlates with the movement of centrosomes towards the short nuclear axis. Recruitment of Dynein to the cortex during later stages of mitosis requires activity of the LGN-Gαi-NuMA complex and this can be prevented by inhibiting the activity of Gαi with pertussis toxin (PTx) (Kotak et al., 2012; Woodard et al., 2010). To test whether cortical Dynein-dependent forces are needed to maintain centrosome alignment with the pattern, we treated cells with PTx and followed centrosome movement. Treatment with PTx led to a premature mitotic cell rounding, with centrosomes deviating from the pattern towards the short nuclear axis (Fig. 3J and S6C-E). As a result, at NEB these cells were still able to position centrosomes on the short

nuclear axis (Fig 3K). Thus, we conclude cortical Dynein is required to maintain centrosome alignment with the underlying micropattern prior to mitotic cell rounding.

Centrosome movement to the short nuclear axis requires Arp2/3 activity and Dynein on the Nuclear Envelope

One of the main players involved in centrosome separation is kinesin-5 (Kapoor et al., 2000; Whitehead et al., 1996). To assess whether it is also required to position centrosomes on the short nuclear axis, we treated cells with the small molecule inhibitor of Eg5 (STLC), either when centrosomes were already on opposite sides of the nucleus (Late stage) or when centrosomes were still not fully separated (Early stage) (Fig. S7). As expected, inhibition of Eg5 activity in the early stage significantly decreased pole-to-pole distances, preventing centrosomes from reaching opposite sides of the nucleus. This led to a defect in centrosome positioning on the short nuclear axis. However, if Eg5 activity was blocked when centrosomes were already on opposite sides of the nucleus, centrosomes were able to move towards the short nuclear axis. Interestingly, this movement only occurred when mitotic cell rounding began. Overall, we concluded that kinesin-5 is required for the separation but not directionality of centrosome movement, which is provided by Dynein.

Next, we determined how centrosomes move towards the short nuclear axis. During our high-resolution, live-cell imaging of HeLa cells expressing Lifeact-mcherry/EB3-GFP, we consistently observed the appearance of subcortical actin ”clouds”, which preceded cell rounding (92% of the cells treated with DMSO and 89% of the cells treated with scrambled RNAi; Fig. 4A, D). The first “cloud” appeared near the nucleus and moved towards one of the tips of the elongated cell after which rounding occurred on that side. A second “cloud” then appeared on the opposite side near the cortex, immediately prior to rounding. Arp2/3-mediated subcortical actin “clouds” were previously described during mitosis (Fink et al., 2011; Mitsushima et al., 2010). We reasoned the clouds we observe during prophase were of a similar nature. As so, we treated cells with a specific inhibitor of Arp2/3 (CK666) or with siRNA for ARPC4. In either case, interfering with Arp2/3 activity induced a loss of the subcortical actin “clouds”, with now only 20% of the cells treated with CK666 and 30% of the cells treated with ARPC4 RNAi having an actin “cloud”. In both these treatments, there was a significant impairment of cell rounding and limited centrosome movement, resulting in a failure to position centrosomes on the short nuclear axis (Fig. 4A-D and S8). To further characterize how the actin clouds affected centrosome motion, we analyzed astral microtubule dynamics using the plusTipTracker software (Applegate et al., 2011). We selected single planes of cells expressing Lifeact-mcherry/EB3-GFP at high spatio-temporal resolution. After treatment with CK666, astral microtubule growth speed and length, as well as the number of growths, were significantly increased when compared to controls (Fig. 4E, F). Moreover, when actin clouds appeared in control cells, a clear decrease in the number of microtubule tips could be observed near the cloud region (Fig. 4E). A recent report proposed that branched actin networks create a physical barrier that blocks microtubule growth (Colin et al., 2018). It is possible that the prophase Arp2/3 subcortical actin “clouds” generate a barrier for microtubules, uncoupling them from the cell cortex. This event, together with the cortical reorganization that occurs during cell rounding, induces motion of the centrosome along the nuclear envelope. If this is correct, we hypothesized that by stabilizing microtubules, centrosomes cannot not move to the short nuclear axis, even in the presence of actin “clouds”. Indeed, by treating cells with nanomolar doses of Taxol,

we were able to interfere with centrosome movement and positioning on the short nuclear axis (Fig. S9). Therefore, we concluded the subcortical actin “clouds” induce a destabilization of the MT network, thus generating centrosome movement.

The cues that ultimately define centrosome positioning may be intrinsic to the prophase nucleus or, in alternative, be provided externally by the cytoskeleton or centrosomes. To separate between these hypotheses, we decided to uncouple all components. It is known that tethering of centrosomes to the NE in prophase requires the activity of NE-associated Dynein. Loading of Dynein occurs by two pathways, which involve RanBP2-BicD2 and Nup133-CENP-F (Bolhy et al., 2011; Splinter et al., 2010). By interfering with one of these factors, we prevent Dynein localization and activity on the NE. Accordingly, when we followed mitotic entry in cells depleted of NudE/NudEL (part of the Nup133-CENP-F pathway), we uncoupled centrosomes from the NE (Fig. 4G and S10A, B). Under these conditions, centrosomes were still able to align with the micropattern during early stages of separation, as measured by theta and phi, indicating that cortical Dynein is still active. However, these cells failed to position centrosomes on the short nuclear axis at NEB (Fig. 4G, H). Likewise, depletion of total Dynein Heavy Chain (DHC) or BicD2 by RNAi also affect centrosome positioning (Fig. S10C, D). Overall, this indicates that centrosome-nuclear coupling is essential to ensure proper centrosome positioning at NEB.

Next, we decided to test whether nuclear-cytoskeletal coupling is necessary for centrosome positioning. The nucleus is physically linked to the cytoskeleton through the LINC complex. To interfere with this, we expressed a dominant negative KASH-GFP mutant, which displaces endogenous Nesprins from the NE, leading to disruption of the LINC complex (Lombardi et al., 2011). Under these conditions, centrosomes were still able to move along the surface of the NE and position on the short nuclear axis at NEB (Fig. S11), indicating that nucleo-cytoskeletal coupling is not required for this process. Rather, this implies that centrosomes need to be attached to the surface of the NE to sense intrinsic cues derived from the prophase nucleus.

Spatial asymmetries in the prophase nucleus determine centrosome positioning

To uncover the nature of the signal on the prophase nucleus that determines centrosome positioning, we decided to we decided to probe for stiffness variability along the nuclear surface by measuring nuclear envelope fluctuations with a temporal resolution of 100msec in HeLa cells expressing the nucleoporin POM121 tagged with GFP (Fig. 5A), using custom-designed MATLAB computational tools. Radial displacement maps were generated for each of the experimental conditions (Fig. 5B), allowing a visual assessment of the overall fluctuations of the NE. Afterwards, we extracted the median contour of the NE and calculated deviations from the median as well as the maximum amplitude for each NE coordinate and time point. Subsequent analysis of fluctuations was done on two regions: one comprising the long nuclear axis, which was aligned with the underlying micropattern (between 330°-30° and 150°-210°; green triangles, Fig. 5A`) and another comprising the short nuclear axis, perpendicular to the pattern (between 60°-120° and 240°-300°; red triangles, Fig. 5A`). Analysis of interphase nuclei revealed significant differences between the long and short nuclear axes both for median fluctuations and maximum amplitude (Fig. 5C and S12A, B). In prophase nuclei, we found an increase in both median fluctuations (Fig. 5D) and maximum amplitudes (Fig S12C), when compared to interphase cells. Similar to what was observed for interphase cells, the overall fluctuation asymmetries were still evident, suggesting structural

differences between the long and short nuclear axes. Previous works identified Lamin A and chromatin as major components regulating the mechanical response of the nucleus (Schreiner et al., 2015; Stephens et al., 2017). Interestingly, Lamin A was proposed to mediate large deformations, whereas heterochromatin levels modulate nuclear stiffness in response to small extensions. To test the contribution of these two components for the asymmetry observed, we decided to deplete Lamin A by RNAi or interfere with mitotic chromosome condensation by treating cells with ICRF-193, a Topoisomerase II (TopoII) inhibitor. Depletion of Lamin A by RNAi significantly increased the median and maximum fluctuation amplitudes for both nuclear axes in interphase (Fig. 5B and S12B). A similar trend was observed for the long and short nuclear axes in prophase cells, both for median fluctuations as well as maximum fluctuation amplitudes (Fig5D and S12D). In both situations however, nuclear fluctuation asymmetries were maintained. These results are consistent with the role of Lamin A in nuclear stiffening. On the other hand, inhibition of TopoII did not affect median nuclear fluctuations or maximum fluctuation amplitude in interphase cells (Fig. S12A, B), but abolished the fluctuation asymmetry between the long and short axes in prophase (Fig. 5B, D and S12D). We then analyzed centrosome behavior following Lamin A RNAi or ICRF193 treatment. We reasoned that, if nuclear fluctuation asymmetries were important for centrosome positioning, then inhibiting TopoII should affect this process. Treatment with ICRF-193 did not affect centrosome separation or mitotic cell rounding (Fig. S13A-C). However, it did affect centrosome positioning on the short nuclear axis at NEB (Fig. 5D and S13). On the contrary, depletion of Lamin A by RNAi did not affect centrosome positioning at NEB, which correlates with the maintenance of nuclear fluctuation asymmetries in this treatment (Fig. 5B, D, F and S13D-G). Overall, these data suggest that chromosome condensation is required to maintain NE asymmetries as cells prepare to enter mitosis and this is essential to determine centrosomes-nuclear axis in prophase.

Given that NE-associated Dynein is required for centrosome positioning on the short nuclear axis and ICRF-193 treatment significantly affected this process, we wondered whether mitotic chromosome condensation impacts Dynein function on the NE. To test this, we performed immunofluorescence analysis of HeLa cells expressing DHC-GFP seeded on line micropatterns. In control prophase cells, we observed a polarized Dynein distribution on the NE, with increased accumulation on the long axis of the nucleus (Fig. 5G, H). This is in apparent contrast with previous reports, where no such polarization of Dynein was observed (Baffet et al., 2015; Splinter et al., 2010). However, in those cases detection of Dynein was performed after Nocodazole (Noco) incubation. Accordingly, when we treat our cells with Noco, the polarization of Dynein was lost (Fig. 5G, H). Moreover, depletion of Lamin A did not block Dynein recruitment to the NE but also induced a loss of polarization on the NE (Fig. 5G, I). Importantly, treatment with ICRF-193 significantly affected Dynein recruitment to the NE (Fig. 5G, H), without interfering with BicD2 localization (Fig. S14A). Incubation with Noco, ICRF-193 or DHC RNAi did not affect the structure of the nuclear lamina as visualized by immunostaining of Lamins A/C and B1 (Fig. S14B), reinforcing that chromatin condensation *per se*, is required for Dynein loading on the NE. Overall, our results indicate that Dynein recruitment to the NE requires chromosome condensation and that Lamin A and microtubules are necessary to restrict its spatial distribution.

Centrosome positioning on the short nuclear axis facilitates spindle assembly

Previous works reported that centrosome separation affects mitotic efficiency (Kaseda et al., 2012; Silkworth et al., 2012). Therefore, we decided to test whether centrosome positioning on the short nuclear axis could affect spindle assembly efficiency. For that purpose, we imaged HeLa H2B-GFP/tubulin-RFP cells seeded on FBN or PLL and followed their mitotic progression (Fig. 6A). For each cell, we determined centrosome positioning, mitotic timing and missegregation events. As expected, we found that seeding cells on PLL affected centrosome positioning on the short nuclear axis at NEB, when compared to cells seeded on FBN (51% of cells on PLL and 72% of cells on FBN; Fig. 6C). Likewise, on PLL we observed a significant increase in the proportion of cells which failed to separate centrosomes to opposite sides of the nucleus when compared to FBN ("incomplete separation"; 23% of cells on PLL and 8% of cells on FBN). We reasoned that, if centrosome positioning is important for mitotic fidelity, then cells growing on PLL would show an increased frequency of missegregation events. Indeed, cells seeded in PLL had an increased percentage of mitotic errors (19.2%) when compared to FBN (5.7%). These errors were caused in cells that entered mitosis with incomplete centrosome separation and were mainly lagging DNA (Fig. 6C and S15B). Importantly, we did not observe any missegregation event when cells placed centrosomes on the short nuclear axis. Therefore, we concluded that centrosome positioning on the short nuclear axis at NEB increases chromosome segregation fidelity.

Next, we determined whether centrosome positioning affects mitotic timing (Fig. 6B and S15A). Because the number of cells with incorrect centrosome positioning on FBN was too low to perform robust statistics on this parameter, we proceeded our analysis using PLL cells only. Quantification of mitotic timings showed that PLL cells which separated centrosomes, but failed to position them on the short nuclear axis, had a significant mitotic delay ("other nuclear axis"; 72±29 min), when compared to cells with the correct centrosome positioning ("short nuclear axis; 40±18min). This was due to delays both in metaphase chromosome alignment, as well as in anaphase onset (Fig. S15A). Interestingly, cells with incomplete centrosome separation did not show a significant mitotic delay, even though they generated most of the observed missegregation events (Fig. 6B and S15A). Overall, these results suggest that cells with incomplete centrosome separation likely generate lagging chromosomes which are invisible to the Spindle Assembly Checkpoint (SAC), which would be consistent with increased frequencies of missegregation events that do not delay in mitosis (Gregan et al., 2011).

To further confirm whether centrosome positioning on the short nuclear axis is important for mitotic efficiency, we treated cells seeded on FBN with CK666, because we showed that this treatment significantly affects centrosome movement, but not separation (Fig. 4). We reasoned that CK666-treated cells may have a delay in mitosis, without increasing the frequency of missegregation events. Indeed, these cells showed an increased proportion of centrosome misplacement and increased mitotic timing, which could be attributed to a delay in anaphase onset (Fig. 6E, F and S15C). However, this did not increase the frequency of missegregation events, which depended on centrosome separation efficiency (Fig. 6G and S15D). To sum up, our results show that centrosome positioning on the short nuclear axis is essential to ensure timely and efficient progression through mitosis.

Discussion:

The manner in which the mitotic spindle is assembled has clear implications for the fidelity of chromosome segregation. In fact, events such as delays in centrosome separation (Kaseda et al., 2012; Silkworth et al., 2012) or alterations in spindle geometry (Ganem et al., 2009) have been proposed to cause chromosomal instability (CIN). Therefore, a clear understanding of the mechanisms that regulate centrosome separation and bipolar spindle assembly is critical to determine the causes underlying CIN.

Several reports indicate that centrosome separation occurs independently of NEB, which led to the proposal of two concurrent pathways for spindle assembly. In the “P pathway”, centrosome separation is completed before NEB, and in the “PM pathway”, centrosomes separate only after NEB (Kaseda et al., 2012; Rattner and Berns, 1976). It is intriguing why cells would enter mitosis under less favorable conditions such as those observed in the “PM pathway”, as this potentiates the occurrence of chromosome missegregation (Silkworth et al., 2012). Our work sheds light into this problem by showing that under more physiological conditions such as those provided by FBN, centrosome separation occurs prior to NEB, thereby ensuring faithful chromosome segregation. This is in agreement with a recent report that highlights the relevance of cell-matrix interactions for chromosome segregation (Knouse et al., 2018). What could justify the bias towards the “P pathway” when cells are placed in FBN? Larger cell areas correlate with Focal Adhesion assembly and increased cytoskeletal tension (Chen et al., 2003). Our data shows that cells on FBN have larger areas when compared to their PLL counterparts, reflecting an increase in cytoskeletal tension and favoring kinesin-5-dependent centrosome separation. The manner in which cytoskeletal tension feeds back on kinesin-5 to drive timely centrosome separation remains to be determined.

After the initial separation, centrosome movement is oriented along the tension axis. We confirmed these observations by directly measuring traction force patterns and by manipulating cytoskeletal tension. As expected, in conditions of high tension such as when a constitutively active Rap1 mutant is expressed (Freeman et al., 2017), centrosomes are forced to maintain alignment with the underlying micropattern. One interesting possibility is that distribution of cortical force generators during prophase is biased to create a tension axis. In fact, it was proposed that the extracellular matrix geometry can determine the distribution of cortical force generators to regulate metaphase spindle positioning (Fink et al., 2011; Thery et al., 2007). One of the stronger candidates is cortical Dynein, which has been shown to act as a centrosome-centering factor in vitro (Laan et al., 2012) and in interphase cells (Burakov et al., 2003), but also acts as part of a spindle positioning mechanism in metaphase cells (Kiyomitsu and Cheeseman, 2012; Kotak et al., 2012). Our results confirm that cortical Dynein is indeed distributed according to the underlying micropattern and is required to orient centrosome separation axis in the early stages of separation, likely by binding and stabilizing microtubules plus-ends (Hendricks et al., 2012).

One of the major findings of our work is that centrosomes always “search” for the short nuclear axis at NEB. However, initial centrosome separation occurs along the long cellular axis which is tightly coupled with the long nuclear axis (Versaevel et al., 2012). Therefore, an uncoupling between the cytoskeleton and the nucleus should occur to allow correct centrosome-nucleus orientation during prophase. This uncoupling is achieved when cells reorganize their cytoskeleton in preparation for mitosis. During this process, adhesion complexes are remodeled (Dao et al., 2009; Lancaster et al., 2013)

and cell margins retract (Maddox and Burridge, 2003) to allow efficient spindle assembly (Lancaster et al., 2013). Recent observations have demonstrated how adhesion complexes (Jones et al., 2018) and traction forces (Uroz et al., 2018; Vianay et al., 2018) decrease in G2 as cells prepare to enter mitosis. Therefore, it is likely that mitotic cell rounding, coupled with cell-matrix adhesion disassembly, lead to a decrease in contractile energy, releasing centrosomes from the main traction axis and allowing them to be correctly positioned. During this process, Arp2/3-mediated actin "clouds" act as a physical barrier for microtubules, preventing them from reaching the cell cortex. This fits nicely with recent data that showed how a branched actin network efficiently blocks microtubule growth *in vitro* (Colin et al., 2018). As a result, these actin "clouds" could generate a symmetry break on the radial array of centrosomal microtubules which, coupled with cell rounding, trigger motion of the centrosomes along the nuclear envelope, through the action of NE-associated Dynein.

It is unlikely that centrosome movement along the NE surface *per se* could justify the preferential centrosome-nuclear axis observed at NEB. Moreover, when we induce premature cell rounding, block actomyosin contractility or uncouple the nucleus from the cytoskeleton using a dominant-negative KASH construct, centrosomes are still positioned on the short nuclear axis. These observations strongly suggest that an intrinsic property of the nucleus provides the cues for centrosome positioning during prophase. Here, we propose that the mechanical properties of the prophase nucleus could provide such cues. During interphase, the mechanical response of the nucleus relies on the chromatin condensation state (Stephens et al., 2017), Lamin A levels (Buxboim et al., 2017) and also on the interaction of heterochromatin with the nuclear membrane (Schreiner et al., 2015). Moreover, the condensation state of chromatin in interphase determines its own stiffness (Pajerowski et al., 2007) and also nuclear stiffness (Chalut et al., 2012; Mazumder et al., 2008). Both chromatin and the nuclear lamina are extensively remodeled during prophase, as mitotic chromosomes condense (Antonin and Neumann, 2016) and Lamin A is released into the nucleoplasm (Georgatos et al., 1997). This suggests that the mechanical properties of the prophase nucleus are different from interphase. Accordingly, we showed that prophase cells have increased nuclear fluctuations when compared to interphase cells, correlating with the timing of Lamin A removal from the lamina (Georgatos et al., 1997) and with previous data showing that higher Lamin A levels correlate with stiffer nuclei and decreased nuclear fluctuations (Chu et al., 2017). We also determined that these fluctuations were unevenly distributed along the NE and depended on mitotic chromosome condensation, but not Lamin A. Importantly, chromosome condensation is also required for Dynein loading on the NE and ultimately determining correct centrosome positioning. Accumulation of Dynein on the NE depends on two concurrent pathways which are under the regulation of CDK1 (Baffet et al., 2015) and rely on RanBP2-BicD2 (Splinter et al., 2010) and Nup133-CENP-F (Bolhy et al., 2011). In fact, BicD2 recruitment alone is sufficient to load Dynein on the NE (Baffet et al., 2015). Here, we propose that Dynein is sensitive to the mechanical properties of the nucleus and can be uncoupled from BicD2, as we show for the ICRF-193 treated cells. Therefore, while Dynein loading on the NE requires chromosome condensation, its subsequent polarized distribution is sensitive to the tension state of the nucleus and requires microtubules and Lamin A.

In summary, our data reveals that positioning of centrosomes on the short nuclear axis depends on an interplay of external and internal signals to ensure mitotic fidelity. While cytoskeletal tension, through cortical motors, defines the initial centrosome separation axis, subsequent cytoskeletal reorganization coupled with mitotic chromosome

condensation, provides an internal mechanical signal to determine the axis of orientation at NEB. We propose that positioning on the short nuclear axis would ensure the formation of a spindle "scaffold", maximizing exposure of kinetochores to microtubules (Lancaster et al., 2013) and allowing faster capture and orientation of chromosomes (Magidson et al., 2011), while minimizing the probability of generating erroneous attachments.

Acknowledgments:

The authors would like to thank Iain Cheeseman for the HeLa LC8-GFP cell line, Alex Bird for the HeLa DHC-GFP cell line and Katharine Ullman for the HeLa POM121-3xGFP/H2B-mCherry cell line. The authors thank Christophe Guilluy for providing the pEGFP-KASH construct and Jean de Gunzburg for the pRK5-Rap1[Q63E] construct. We thank all members of the CID lab for discussions and suggestions. The authors are grateful to Bernardo Orr and António Pereira for critical reading of the manuscript. This work was funded by grants from FEDER - Fundo Europeu de Desenvolvimento Regional funds through the COMPETE 2020 - Operacional Programme for Competitiveness and Internationalization (POCI), Portugal 2020, and by Portuguese funds through FCT - Fundação para a Ciência e a Tecnologia/Ministério da Ciência, Tecnologia e Ensino Superior in the framework of the project PTDC/BEX-BCM/1758/2014 (POCI-01–0145-FEDER-016589). This work was also partially supported by a grant PHC-Pessoa Campus France/Fundação para a Ciência e Tecnologia. V.N. is supported by grant PD/BD/135545/2018 from the BiotechHealth FCT-funded PhD program. M.D. is supported by grant PD/BD/135548/2018 from the BiotechHealth FCT-funded PhD program. Work in the laboratory of H.M. is funded by the European Research Council (ERC) under the European Union's Horizon 2020 research and innovation program (grant agreement No 681443).

Author contributions:

V.N., M.D and J.G.F. designed and performed experiments. E.V., I.W. and M.B. performed and analyzed TFM experiments. N.C. was involved in setting up the micropatterning technique. P.A. developed all MATLAB computational tools. The manuscript was written primarily by J.G.F. and V.N, with significant input by M.P. and H.M. J.G.F. and H.M obtained funding and provided resources.

Declaration of interests: The authors declare no conflict of interest.

References:

Antonin, W., and Neumann, H. (2016). Chromosome condensation and decondensation during mitosis. Current opinion in cell biology *40*, 15-22.

Applegate, K.T., Besson, S., Matov, A., Bagonis, M.H., Jaqaman, K., and Danuser, G. (2011). plusTipTracker: Quantitative image analysis software for the measurement of microtubule dynamics. J Struct Biol *176*, 168-184.

Azioune, A., Storch, M., Bornens, M., Thery, M., and Piel, M. (2009). Simple and rapid process for single cell micro-patterning. Lab on a chip *9*, 1640-1642.

Baffet, A.D., Hu, D.J., and Vallee, R.B. (2015). Cdk1 Activates Pre-mitotic Nuclear Envelope Dynein Recruitment and Apical Nuclear Migration in Neural Stem Cells. Developmental cell *33*, 703-716.
Beaudouin, J., Gerlich, D., Daigle, N., Eils, R., and Ellenberg, J. (2002). Nuclear envelope breakdown proceeds by microtubule-induced tearing of the lamina. Cell *108*, 83-96.
Bolhy, S., Bouhlel, I., Dultz, E., Nayak, T., Zuccolo, M., Gatti, X., Vallee, R., Ellenberg, J., and Doye, V. (2011). A Nup133-dependent NPC-anchored network tethers centrosomes to the nuclear envelope in prophase. The Journal of cell biology *192*, 855-871.
Burakov, A., Nadezhdina, E., Slepchenko, B., and Rodionov, V. (2003). Centrosome positioning in interphase cells. The Journal of cell biology *162*, 963-969.
Buxboim, A., Irianto, J., Swift, J., Athirasala, A., Shin, J.W., Rehfeldt, F., and Discher, D.E. (2017). Coordinated increase of nuclear tension and lamin-A with matrix stiffness outcompetes lamin-B receptor that favors soft tissue phenotypes. Molecular biology of the cell *28*, 3333-3348.
Chalut, K.J., Hopfler, M., Lautenschlager, F., Boyde, L., Chan, C.J., Ekpenyong, A., Martinez-Arias, A., and Guck, J. (2012). Chromatin decondensation and nuclear softening accompany Nanog downregulation in embryonic stem cells. Biophysical journal *103*, 2060-2070.
Chen, C.S., Alonso, J.L., Ostuni, E., Whitesides, G.M., and Ingber, D.E. (2003). Cell shape provides global control of focal adhesion assembly. Biochemical and biophysical research communications *307*, 355-361.
Chu, F.Y., Haley, S.C., and Zidovska, A. (2017). On the origin of shape fluctuations of the cell nucleus. Proceedings of the National Academy of Sciences of the United States of America *114*, 10338-10343.
Colin, A., Singaravelu, P., Thery, M., Blanchoin, L., and Gueroui, Z. (2018). Actin-Network Architecture Regulates Microtubule Dynamics. Current biology : CB *28*, 2647-2656 e2644.
Cramer, L.P., and Mitchison, T.J. (1997). Investigation of the mechanism of retraction of the cell margin and rearward flow of nodules during mitotic cell rounding. Molecular biology of the cell *8*, 109-119.
Cytrynbaum, E.N., Scholey, J.M., and Mogilner, A. (2003). A force balance model of early spindle pole separation in Drosophila embryos. Biophysical journal *84*, 757-769.
Dao, V.T., Dupuy, A.G., Gavet, O., Caron, E., and de Gunzburg, J. (2009). Dynamic changes in Rap1 activity are required for cell retraction and spreading during mitosis. Journal of cell science *122*, 2996-3004.
Fink, J., Carpi, N., Betz, T., Betard, A., Chebah, M., Azioune, A., Bornens, M., Sykes, C., Fetler, L., Cuvelier, D.*, et al.* (2011). External forces control mitotic spindle positioning. Nature cell biology *13*, 771-778.
Freeman, S.A., Christian, S., Austin, P., Iu, I., Graves, M.L., Huang, L., Tang, S., Coombs, D., Gold, M.R., and Roskelley, C.D. (2017). Applied stretch initiates directional invasion through the action of Rap1 GTPase as a tension sensor. Journal of cell science *130*, 152-163.
Ganem, N.J., Godinho, S.A., and Pellman, D. (2009). A mechanism linking extra centrosomes to chromosomal instability. Nature *460*, 278-282.
Georgatos, S.D., Pyrpasopoulou, A., and Theodoropoulos, P.A. (1997). Nuclear envelope breakdown in mammalian cells involves stepwise lamina disassembly and microtubule-drive deformation of the nuclear membrane. Journal of cell science *110 (Pt 17)*, 2129-2140.
Gregan, J., Polakova, S., Zhang, L., Tolic-Norrelykke, I.M., and Cimini, D. (2011). Merotelic kinetochore attachment: causes and effects. Trends in cell biology *21*, 374-381.

Hendricks, A.G., Lazarus, J.E., Perlson, E., Gardner, M.K., Odde, D.J., Goldman, Y.E., and Holzbaur, E.L. (2012). Dynein tethers and stabilizes dynamic microtubule plus ends. Current biology : CB *22*, 632-637.
Jones, M.C., Askari, J.A., Humphries, J.D., and Humphries, M.J. (2018). Cell adhesion is regulated by CDK1 during the cell cycle. The Journal of cell biology *217*, 3203-3218.
Kapoor, T.M., Mayer, T.U., Coughlin, M.L., and Mitchison, T.J. (2000). Probing spindle assembly mechanisms with monastrol, a small molecule inhibitor of the mitotic kinesin, Eg5. The Journal of cell biology *150*, 975-988.
Kaseda, K., McAinsh, A.D., and Cross, R.A. (2012). Dual pathway spindle assembly increases both the speed and the fidelity of mitosis. Biology open *1*, 12-18.
Kiyomitsu, T., and Cheeseman, I.M. (2012). Chromosome- and spindle-pole-derived signals generate an intrinsic code for spindle position and orientation. Nature cell biology *14*, 311-317.
Knouse, K.A., Lopez, K.E., Bachofner, M., and Amon, A. (2018). Chromosome Segregation Fidelity in Epithelia Requires Tissue Architecture. Cell *175*, 200-211 e213.
Kotak, S., Busso, C., and Gonczy, P. (2012). Cortical dynein is critical for proper spindle positioning in human cells. The Journal of cell biology *199*, 97-110.
Kunda, P., Pelling, A.E., Liu, T., and Baum, B. (2008). Moesin controls cortical rigidity, cell rounding, and spindle morphogenesis during mitosis. Current biology : CB *18*, 91-101.
Laan, L., Pavin, N., Husson, J., Romet-Lemonne, G., van Duijn, M., Lopez, M.P., Vale, R.D., Julicher, F., Reck-Peterson, S.L., and Dogterom, M. (2012). Cortical dynein controls microtubule dynamics to generate pulling forces that position microtubule asters. Cell *148*, 502-514.
Lancaster, O.M., Le Berre, M., Dimitracopoulos, A., Bonazzi, D., Zlotek-Zlotkiewicz, E., Picone, R., Duke, T., Piel, M., and Baum, B. (2013). Mitotic rounding alters cell geometry to ensure efficient bipolar spindle formation. Developmental cell *25*, 270-283.
Lombardi, M.L., Jaalouk, D.E., Shanahan, C.M., Burke, B., Roux, K.J., and Lammerding, J. (2011). The interaction between nesprins and sun proteins at the nuclear envelope is critical for force transmission between the nucleus and cytoskeleton. The Journal of biological chemistry *286*, 26743-26753.
Maddox, A.S., and Burridge, K. (2003). RhoA is required for cortical retraction and rigidity during mitotic cell rounding. The Journal of cell biology *160*, 255-265.
Magidson, V., O'Connell, C.B., Loncarek, J., Paul, R., Mogilner, A., and Khodjakov, A. (2011). The spatial arrangement of chromosomes during prometaphase facilitates spindle assembly. Cell *146*, 555-567.
Mandal, K., Wang, I., Vitiello, E., Orellana, L.A., and Balland, M. (2014). Cell dipole behaviour revealed by ECM sub-cellular geometry. Nature communications *5*, 5749.
Marchesi, S., Montani, F., Deflorian, G., D'Antuono, R., Cuomo, A., Bologna, S., Mazzoccoli, C., Bonaldi, T., Di Fiore, P.P., and Nicassio, F. (2014). DEPDC1B coordinates de-adhesion events and cell-cycle progression at mitosis. Developmental cell *31*, 420-433.
Mardin, B.R., Isokane, M., Cosenza, M.R., Kramer, A., Ellenberg, J., Fry, A.M., and Schiebel, E. (2013). EGF-induced centrosome separation promotes mitotic progression and cell survival. Developmental cell *25*, 229-240.
Mazumder, A., Roopa, T., Basu, A., Mahadevan, L., and Shivashankar, G.V. (2008). Dynamics of chromatin decondensation reveals the structural integrity of a mechanically prestressed nucleus. Biophysical journal *95*, 3028-3035.
Mitchison, T.J. (1992). Actin based motility on retraction fibers in mitotic PtK2 cells. Cell motility and the cytoskeleton *22*, 135-151.
Mitsushima, M., Aoki, K., Ebisuya, M., Matsumura, S., Yamamoto, T., Matsuda, M., Toyoshima, F., and Nishida, E. (2010). Revolving movement of a dynamic cluster of actin filaments during mitosis. The Journal of cell biology *191*, 453-462.

Pajerowski, J.D., Dahl, K.N., Zhong, F.L., Sammak, P.J., and Discher, D.E. (2007). Physical plasticity of the nucleus in stem cell differentiation. Proceedings of the National Academy of Sciences of the United States of America *104*, 15619-15624.
Prosser, S.L., and Pelletier, L. (2017). Mitotic spindle assembly in animal cells: a fine balancing act. Nature reviews Molecular cell biology *18*, 187-201.
Rattner, J.B., and Berns, M.W. (1976). Centriole behavior in early mitosis of rat kangaroo cells (PTK2). Chromosoma *54*, 387-395.
Salina, D., Bodoor, K., Eckley, D.M., Schroer, T.A., Rattner, J.B., and Burke, B. (2002). Cytoplasmic dynein as a facilitator of nuclear envelope breakdown. Cell *108*, 97-107.
Schreiner, S.M., Koo, P.K., Zhao, Y., Mochrie, S.G., and King, M.C. (2015). The tethering of chromatin to the nuclear envelope supports nuclear mechanics. Nature communications *6*, 7159.
Silkworth, W.T., Nardi, I.K., Paul, R., Mogilner, A., and Cimini, D. (2012). Timing of centrosome separation is important for accurate chromosome segregation. Molecular biology of the cell *23*, 401-411.
Sommi, P., Cheerambathur, D., Brust-Mascher, I., and Mogilner, A. (2011). Actomyosin-dependent cortical dynamics contributes to the prophase force-balance in the early Drosophila embryo. PloS one *6*, e18366.
Splinter, D., Tanenbaum, M.E., Lindqvist, A., Jaarsma, D., Flotho, A., Yu, K.L., Grigoriev, I., Engelsma, D., Haasdijk, E.D., Keijzer, N.*, et al.* (2010). Bicaudal D2, dynein, and kinesin-1 associate with nuclear pore complexes and regulate centrosome and nuclear positioning during mitotic entry. PLoS biology *8*, e1000350.
Stephens, A.D., Banigan, E.J., Adam, S.A., Goldman, R.D., and Marko, J.F. (2017). Chromatin and lamin A determine two different mechanical response regimes of the cell nucleus. Molecular biology of the cell *28*, 1984-1996.
Tanenbaum, M.E., and Medema, R.H. (2010). Mechanisms of centrosome separation and bipolar spindle assembly. Developmental cell *19*, 797-806.
Thery, M., Jimenez-Dalmaroni, A., Racine, V., Bornens, M., and Julicher, F. (2007). Experimental and theoretical study of mitotic spindle orientation. Nature *447*, 493-496.
Thery, M., Racine, V., Pepin, A., Piel, M., Chen, Y., Sibarita, J.B., and Bornens, M. (2005). The extracellular matrix guides the orientation of the cell division axis. Nature cell biology *7*, 947-953.
Uroz, M., Wistorf, S., Serra-Picamal, X., Conte, V., Sales-Pardo, M., Roca-Cusachs, P., Guimera, R., and Trepat, X. (2018). Regulation of cell cycle progression by cell-cell and cell-matrix forces. Nature cell biology *20*, 646-654.
Versaevel, M., Grevesse, T., and Gabriele, S. (2012). Spatial coordination between cell and nuclear shape within micropatterned endothelial cells. Nature communications *3*, 671.
Vianay, B., Senger, F., Alamos, S., Anjur-Dietrich, M., Bearce, E., Cheeseman, B., Lee, L., and Thery, M. (2018). Variation in traction forces during cell cycle progression. Biol Cell *110*, 91-96.
Vignaud, T., Ennomani, H., and Thery, M. (2014). Polyacrylamide hydrogel micropatterning. Methods in cell biology *120*, 93-116.
Whitehead, C.M., Winkfein, R.J., and Rattner, J.B. (1996). The relationship of HsEg5 and the actin cytoskeleton to centrosome separation. Cell motility and the cytoskeleton *35*, 298-308.
Woodard, G.E., Huang, N.N., Cho, H., Miki, T., Tall, G.G., and Kehrl, J.H. (2010). Ric-8A and Gi alpha recruit LGN, NuMA, and dynein to the cell cortex to help orient the mitotic spindle. Molecular and cellular biology *30*, 3519-3530.
Zhai, Y., Kronebusch, P.J., Simon, P.M., and Borisy, G.G. (1996). Microtubule dynamics at the G2/M transition: abrupt breakdown of cytoplasmic microtubules at nuclear envelope breakdown and implications for spindle morphogenesis. The Journal of cell biology *135*, 201-214.

Figure Titles and Legends:

Figure 1: Detailed characterization of mitotic spindle assembly

(A) Selected frames from a HeLa cell expressing EB3-GFP/Lifeact-mCherry seeded on a line micropattern, showing the movement of centrosomes towards the short nuclear axis. Time is in min:sec. Time zero corresponds to NEB. (B) Characterization of centrosome orientation vector in xy (theta; red) and z (phi; blue) for cells expressing EB3-GFP/Lifeact-mCherry seeded on line micropatterns (n=30). Each dot corresponds to individual trajectories for a specific centrosome vector. Lines represent average values, which were used to plot graph in Fig. S3 (C) Cell membrane eccentricity during mitotic entry for the same cells shown in (B). Individual dots correspond to a specific time-point extracted from reconstructed cell membranes. Line represents average value and bars represent standard deviation. Average values were used to plot graph in Fig. S3. (D) Representative kymograph extracted from cell expressing Lifeact-mCherry seeded on a line micropattern, showing cell rounding during mitotic entry. (E) Quantification of the cell rounding behavior for cells seeded on a line micropattern. The majority of cells exhibits asymmetric rounding. (F) Characterization of the cortical retraction velocity (μm/min) and cortical width (μm) for cells seeded on line micropatterns. (G) Polar plot quantifying centrosome positioning (red circles) relative to the short nuclear (blue ellipse) at NEB for cells seeded on line micropatterns. (H) Quantification of centrosome separation behavior for cells seeded on line micropatterns.

Figure 2: Geometrical control of spindle assembly

(A) HeLa cells expressing EB3-GFP/Lifeact-mCherry or H2B-GFP/alpha-tubulin-RFP were seeded on large circles (700μm^2; n=32), small circles (80μm^2; n=16) or rectangles (500μm^2; n=36) and imaged during mitotic entry on a spinning-disc microscope with a 20sec time-lapse. Scale bar 10μm. Polar plot quantifying centrosome positioning relative to the short nuclear at NEB for cells seeded on Large circles (B), Small circles (C) and rectangles (D). Characterization of centrosome orientation vector in xy (theta; red) and z (phi; blue) for cells expressing EB3-GFP/Lifeact-mCherry seeded on on Large circles (E), Small circles (F) and rectangles (G). Each dot corresponds to individual trajectories for a specific time point. Lines represent average values.

Figure 3: Tension determines the initial centrosome separation axis

(A) Frames from a movie of a HeLa cell expressing H2B-GFP/alpha-tubulin-RFP (left panel) seeded on a PAA hydrogel with a rectangle micropattern. Right panel corresponds to brightfield (BF) image overlaid with the corresponding traction force map (red arrows). Red line corresponds to the axis of symmetry. Green line corresponds to the main direction of the force dipole. Magenta line corresponds to the secondary direction of the force dipole. (B) Traction force orientation for cells on rectangles (n=14). (C) Correlation between centrosome orientation axis (theta; red) and traction axis (blue). (D) Correlation between contractile energy (EC; blue) and cell area (red) for cells seeded on rectangles. (E) Selected frames from time-lapse movies of HeLa cells expressing EB3-GFP/Lifeact-mCherry, showing xy, xz, and yz views, seeded on line micropatterns (Mock transfected, n=36; Rap1*, n=30; DMSO, n=39; Y-27632, n=35). Time-lapse is 20sec. Time zero corresponds to NEB. Scale bar, 10μm. (F) Representative chromo-kymographs showing

centrosome movement in controls, Rap1* and Y27632 cells. Centrosome movement in x can be observed by attributing an RGB combination to thin ROI subslices, allowing distinction of objects that colocalize in x. Note how centrosome movement is limited in Rap1* cells and increased in Y27632-treated cells, when compared to controls. Dashed line indicates NEB. Horizontal scale bar, 10μm; vertical scale bar, 100sec. (G) Correlation of cell membrane eccentricity (black), theta (red) and phi (blue) for controls, Rap1* and Y-27632 cells. Plots correspond to averages of graphs on Fig. S6. (H) Polar plots quantifying centrosome positioning relative to the short nuclear at NEB for cells seeded on line micropatterns. (I) HeLa cell expressing LC8-GFP (top panel) showing cortical localization (white arrowheads) and corresponding kymograph with a fire LUT (bottom panel). Dashed line indicates NEB. Horizontal scale bar, 10μm; vertical scale bar, 100 sec. (J) Correlation of cell membrane eccentricity (black), theta (red) and phi (blue). (K) Polar plot quantifying centrosome positioning (red circles) relative to the short nuclear (blue ellipse) at NEB (bottom panel) for cells treated with PTx seeded on line micropatterns (n=31).

Figure 4: Centrosomes move to the short nuclear axis before Nuclear Envelope Breakdown

(A) Kymographs of HeLa cells expressing EB3-GFP/Lifeact-mCherry seeded on line micropatterns (DMSO, n=39; CK666, n=41; Scrambled RNAi, n=22; ARPC4 RNAi, n=34). White arrowheads in control cells indicate the appearance of subcortical actin clouds. Black arrowheads indicate centrosomes. Dashed line indicates NEB. Horizontal scale bar, 10μm; vertical scale bar, 100 sec. Interfering with Arp2/3 function eliminates the subcortical actin clouds and limits centrosome movement. (B) Correlation of cell membrane eccentricity (black), theta (red) and phi (blue) for cells treated with CK666. Plots correspond to averages of graphs on Fig. S8. Polar plot quantifying centrosome positioning relative to the short nuclear at NEB for cells seeded on line micropatterns treated with CK666 (C) or ARPC4 RNAi (D). (E) Quantification of the percentage of cells with actin clouds for CK666-treated and ARPC4 RNAi cells and respective controls. (F) High temporal resolution kymographs for controls and CK666-treated cells. Top panel represents a control cell, imaged with a 2sec time-lapse. Dashed box corresponds to right panel showing EB3 comets with a fire LUT. Middle panel represents a control cell, imaged with a 500ms time-lapse. Note how appearance of subcortical actin clouds (asterisks) decreases the density of EB3 comets near the cortex. Bottom panel represents a cell treated with CK666 imaged with a 2sec time-lapse. Note the absence of actin clouds. (G) Microtubule dynamics parameters for control (79899 tracks from 41 cells) and CK666-treated cells (79957 tracks from 23 cells; *** $p<0.001$). Top panel corresponds to the number of growths, middle panel corresponds to microtubule growth speed (μm/min) and bottom panel corresponds to microtubule growth length (μm). (H) Top panel shows a HeLa cell expressing H2B-GFP/alpha-tubulin-RFP treated with NudE/NudEL RNAi. Note how centrosomes are detached from the nucleus (white arrowheads). Scale bar, 10μm. Bottom panels show a HeLa cell expressing EB3-GFP/Lifeact-mCherry treated with NudE/NudEL RNAi. The dashed ellipse is highlighting the nuclear shape. Cells were filmed with a 20sec time-lapse. Time zero corresponds to NEB. Scale bar 10μm. (I) Correlation of cell membrane eccentricity (black), theta (red) and phi (blue). Plots correspond to averages of graphs on Fig. S10. (J) Polar plot quantifying centrosome positioning relative to the short nuclear at NEB for cells treated with NudE/NudEL RNAi (n= 36), seeded on line micropatterns.

Figure 5: Spatial asymmetries of the prophase nucleus determine centrosome positioning

(A) Images of HeLa cells expressing POM121-3xGFP/H2B-mCherry/SiR-tubulin. Scale bar, 10μm. Insets represent maximum temporal projections of POM121. (A`) Diagram depicting regions that were selected for nuclear fluctuation analysis. Long nuclear axis corresponds to green triangles and short nuclear axis corresponds to red triangles. (B) Radial displacement maps for interphase (left panels) and prophase (right panels) of control cells (n=40 for interphase and n=39 for mitosis), cells treated with ICRF-193 (n=15 for interphase and n=16 for mitosis) and cells treated with Lamin A RNAi (n=28 for interphase and n=25 for mitosis). This representation allows analysis of nuclear membrane displacements along the surface of the nuclear envelope over time. (C) Quantification of the standard deviation from the median for nuclear fluctuation on the long and short nuclear axes in control interphase and prophase cells (top panel; *** $p<0.001$). (D) Analysis of standard deviation from the median for prophase nuclear fluctuations for controls (n=39), ICRF-193 (n=16), Lamin A RNAi (n=25) and Nocodazole (Noc; n=32) (**$p<0.01$; * $p<0.05$; n.s. - not significant). Polar plots quantifying centrosome positioning (red circles) relative to the short nuclear (blue ellipse) at NEB for cells treated with ICRF-193 (E; n=27) and Lamin A RNAi (F; n=33). (G) Quantification of NE-associated DHC fluorescence intensity in the long and short nuclear axes of prophase cells for controls (n=31), ICRF-193 (n=30), Lamin A RNAi (n=31) and Noco (n=31) (*** $p<0.001$; n.s. - not significant). (H) Representative images of immunofluorescence analysis of DHC-GFP, Lamin B1 (Alexa 594), alpha-tubulin (Alexa 647) and DAPI for controls, ICRF-193 and Noco. Images correspond to deconvoluted, maximal intensity projections. Bottom panels show merged image. Note the asymmetric localization of DHC-GFP on the nuclear envelope of control prophase cells (white arrowhead). Scale bar, 10μm. (I) Representative images of immunofluorescence analysis of DHC (Alexa488), Lamin A (Alexa 594), alpha-tubulin (Alexa 647) and DAPI for cells treated with Lamin A RNAi. Images correspond to deconvolved, maximal intensity projections. Bottom panels show merged image.

Figure 6: Centrosome positioning on the short nuclear axis facilitates spindle assembly

(A) Frames from movies of HeLa cells expressing H2B-GFP/alpha-tubulin-RFP during mitosis. Top panel represents a cell with centrosomes on short nuclear axis at NEB, middle panel represents a cell with centrosomes on a random nuclear axis and bottom panel represents a cell with incomplete centrosomes separation. Time-lapse is 2 min. Scale bar, 5μm. (B) Timing from NEB to anaphase onset for cells seeded on FBN (n=35) or PLL (n=47), according to their centrosome orientation pattern (green, centrosomes separated on the “short nuclear axis”; blue, centrosomes separated on “other nuclear axis”; red, centrosomes with “incomplete centrosome separation”). Cells with centrosomes “on other nuclear axis” at NEB have a delay in mitosis, when compared to controls (*** $p<0.001$; n.s. - not significant). (C) Quantification of the proportion of cells which place centrosomes on short nuclear axis (green), other nuclear axis (blue) or have incomplete separation (red) at NEB, depending on the coating used (FBN or PLL). (D) Quantification of the percentage and type of missegregation events, depending on the coating (FBN or PLL) and the mode of centrosome orientation. (E) Timing from NEB to

anaphase onset for cells seeded on FBN that were treated with DMSO (n=40) or CK666 (n=37), according to their centrosome orientation pattern (green, centrosomes separated on the “short nuclear axis”; blue, centrosomes separated on “other nuclear axis”; red, centrosomes with “incomplete centrosome separation”). Cells treated with CK666 that have separated centrosomes to an incorrect nuclear axis at NEB have a delay in mitosis, when compared to controls (** $p<0.01$; n.s. - not significant). (F) Quantification of the percentage of missegregation events for cells on FBN that were treated with DMSO or CK666. Note the increase in the proportion of cells that do not place centrosomes on the short nuclear axis. (G) Quantification of the percentage and type of missegregation events, for cells treated with DMSO or CK666, depending on the mode of centrosome orientation.

STAR methods:

Cell lines and transfections

Cell lines were cultured in Dulbecco's Modified Eagle Medium (DMEM; Life Technologies) supplemented with 10% fetal bovine serum (FBS; Life Technologies) and grown in a 37˚C humidified incubator with 5% CO2. HeLa N-FLAP DYNC1H1 siRES2 (Clone #20), HeLa LC8-GFP and HeLa POM121-3xGFP/H2B-mCherry cell lines were a kind gift from Alex Bird, Iain Cheeseman and Katharine Ullman, respectively. HeLa cell line expressing histone H2B-GFP/α-tubulin-RFP was generated in our lab using lentiviral vectors. For this purpose, HEK293T cells at 50%-70% confluence were co-transfected with lentiviral packaging vectors (16.6 µg of Pax2 and 5.6 µg of pMD2) and 22.3 µg of H2B-GFP or α-tubulin-RFP plasmids, using 30 µg of Lipofectamine 2000 (Life Technologies). 3-7 days after transfection, the virus-containing supernatant was collected, centrifuged, filtered and stored at –80°C. HeLa parental cells were then transduced with each lentivirus in the presence of polybrene (1:1000) in standard culture media, for 24 h. The lentiviruses produced were used individually and subsequently, giving time for the cells to recover between transductions. 5–7 days after the second transduction H2B-GFP/α-tubulin-RFP double-positive cells were isolated by fluorescence-activated cell sorting (FACS; FACS Aria II). For transient overexpression of pEGFP-KASH (a kind gift from Christophe Guilluy) or pRK5-Rap1[Q63E] plasmids (a kind gift from Jean de Gunzburg), cells were transfected with the corresponding plasmid using Lipofectamine 2000 (Life Technologies). Briefly, cells at 50%–70% confluence were incubated for 6 h with 5 µl of Lipofectamine 2000 and 0.6 µg/ml of DNA. DNA-lipid complexes were previously diluted in Opti-Minimal Essential Medium (Opti-MEM; Alfagene) and incubated for 30 min before adding to the cells. Prior to and during transfection, cell medium was changed to a reduced serum medium (DMEM supplemented with 5% FBS). Cells were analysed 48 h after transfection.

Micro-patterning

Micro-patterns to control individual cell shape and adhesion pattern were produced as previously described (Azioune et al., 2009). Briefly, glass coverslips (22 X 22mm No. 1.5, VWR) were activated with plasma (Zepto Plasma System, Diener Electronic) for 1 min and incubated with 0.1 mg/ml of PLL(20)-g[3,5]-PEG(2) (SuSoS) in 10 mM HEPES at pH 7.4, for 1 h, at RT. After rinsing and air-drying, the coverslips were placed on a synthetic quartz photomask (Delta Mask), previously activated with deep-UV light (PSD-

UV, Novascan Technologies) for 5 min. 3 µl of MiliQ water were used to seal each coverslip to the mask. The coverslips were then irradiated through the photomask with the UV lamp for 5 min.. Afterwards, coverslips were incubated with 25 µg/ml of fibronectin (Sigma-Aldrich) and 5 µg/ml of Alexa546 or 647-conjugated fibrinogen (Thermo Fisher Scientific) in 100 mM NaHCO3 at pH 8.6, for 1 h, at RT. Cells were seeded at a density of 50 000 cells/coverslip and allowed to spread for ~10-15h before imaging. When necessary, non-attached cells were removed by changing the medium ~2h-5h after seeding. The following patterns were used in this work: line (10 µm width), rectangle (projected area of 500µm^2), small circle (projected area of 80 µm^2) and large circle (projected area of 700 µm^2).

Drug treatments

To inhibit the activity of the Arp2/3 complex we used 100 µM of CK666 (Tocris Bioscience). To block ATPase activity of myosin we used 50 µM of para-nitro-blebbistatin (Optopharma). ROCK inhibitor Y-27632 was used at a concentration of 20 µM (Sigma-Aldrich). Pertussis toxin (PTx) was used at 40 nM (Merck). Chromosome condensation was impaired by adding 10 µM of the Topoisomerase II inhibitor - ICRF-193 (Merck-Millipore) to the cell medium. To interfere with the microtubule cytoskeleton we used low doses of taxol (2 nM) or nocodazole (20 nM) (Sigma-Aldrich). All the drugs used were added to the culture medium 30 min-1h before live-cell imaging or fixation. Control cells were treated with DMSO (Sigma-Aldrich) only.

RNAi experiments

Cells were transfected with small interfering RNAs (siRNAs) using Lipofectamine RNAi Max (Life Technologies), following the manufactures instructions. Specifically, 5µl of Lipofectamine and 20 nM of each siRNA were diluted and incubated in Opti-MEM (Alfagene) for 30 min. The siRNA-lipid complexes were then added to 50%–70% confluence cells cultured, during transfection (6 h), in reduced serum medium (DMEM supplemented with 5% FBS). Commercial ON-TARGETplus siRNAs (Dharmacon) were used for Lamin-A/C (set of 4: 5'-GAAGGAGGGUGACCUGAUA-3', 5'-UCACAGCACGCACGCACUA-3', 5'-UGAAAGCGCGCAAUACCAA-3' and 5'-CGUGUGCGCUCGCUGGAAA-3'), BICD2 (SMARTpool: 5'-AGACGGAGCGCGAACAGAA-3', 5'-UAAAGAAGGUGAGCGACGU-3', 5'-GCAAGUACCAUGUGGCUGU-3' and 5'-GGAAGGUGCUAGAGCUGCA-3') and ARPC4 (set of 4: 5'-GAACUUCUUUAUCCUUCGA-3', 5'-UAAACCAUCUGGCUGGAUC-3', 5'-GAAGAGUUCCUUAAGAAUU-3' and 5'-GAGAUGAAGCUGUCAGUCA-3') depletions. For Dynein Heavy Chain (DHC) depletion the following oligos were ordered 5′-GAACUAGACUUGGUUAAUU-3′ and 5′-AAUUAACCAAGUCUAGUUC-3′. For combined NudE/NudEL depletion the following oligos were ordered 5`-GCUUGAAUCAGGCCAUCGA-3` and 5`-UCGAUGGCCUGAUUCAAGC-3` for NudE and 5`-GGAUGAAGCAAGAGAUUUA-3`and 5`-UAAAUCUCUUGCUUCAUCC-3`for NudEL. ForBoth commercial ON-TARGETplus non-targeting Pool siRNAs (SMARTpool: 5´-UGGUUUACAUGUCGACUAA-3', 5'-UGGUUUACAUGUUGUGUGA-3', 5'-UGGUUUACAUGUUUUCUGA-3' and 5'-UGGUUUACAUGUUUUCCUA-3') and mock transfections were used as controls. For all siRNAs used, cells were analysed 72 h after

transfection. Protein depletion efficiency was monitored by immunoblotting and phenotypic analysis.

Time-lapse microscopy

For time-lapse microscopy, 12-24 h before the experiments $1.5x10^5$ cells were seeded on coverslips coated with FBN (25μg/ml; F1141, Sigma) or PLL (25μg/ml; F1141, Sigma). When micro-patterns were used, $5x10^4$ cells were seeded on coverslips coated with FBN (25μg/ml; F1141, Sigma). Prior to each experiment, cell culture medium was changed from DMEM+10% FBS to Leibovitz's-L15 medium (Life Technologies) supplemented with 10% FBS and Antibiotic-Antimycotic 100X (AAS; Life Technologies). When SiR-dyes were used, they were added to the culture medium 30min-1h before acquisition (20nM Sir-tubulin or 10nM Sir-DNA; Spirochrome). Live-cell imaging was performed using temperature-controlled Nikon TE2000 microscopes equipped with a modified Yokogawa CSU-X1 spinning-disc head (Yokogawa Electric), an electron multiplying iXon+ DU-897 EM-CCD camera (Andor) and a filter-wheel. Three laser lines were used for excitation at 488, 561 and 647 nm. For nuclear pore fluctuation and microtubule dynamics analysis, an oil-immersion 100x 1.4 NA Plan-Apo DIC (Nikon) was used, whereas for all the remaining experiments was used an oil-immersion 60x 1.4 NA Plan-Apo DIC (Nikon). Image acquisition was controlled by NIS Elements AR software. For centrosome tracking 17-21 z-stacks with a 0.5μm separation were collected every 20 sec. For mitotic timing quantifications, 13 z-stacks with a 0.7 μm separation were collected every 2 min. For microtubule dynamics and nuclear envelope fluctuation measurements a single z-stack was collected every 500 msec or 100 msec, respectively.

Quantitative analysis of centrosomes, cell membrane and nucleus membrane

Detailed quantitative analysis of centrosomes location and membranes topology (cell and nucleus) was performed using custom made MATLAB scripts (The MathWorks Inc., USA; R2018a). The image analysis took advantage of the different labeling for centrosomes, cell membrane and nuclear membrane. The scripts were separated into three modules with specific workflows: i) centrosomes tracking, ii) nuclear and cellular membrane reconstruction, and iii) nuclear membrane surface dynamics.

Tracking of centrosomes position/trajectories was performed in three-dimensional (3D) space using image stacks with a pixel size of 0.190μm and z-step of 0.7μm. Images were pre-processed using a Laplacian of Gaussian filter with a user-defined kernel size, associated with the centrosome radius in pixels. Image segmentation was performed using Otsu's method, and morphological operators were used to improve the mask and obtain the centrosomes 3D coordinates. Error correction methods, such as automatic thresholding adjustment or in the limit frame elimination, were implemented to take care of frames where the standard method was unable to uniquely identify 2 centrosomes. For the visualization of the centrosomes trajectories (space and time), the centrosomes coordinates were interpolated using cubic splines. Different metrics, such as the distance between centrosomes (pole-to-pole), were calculated to analyze and characterize the trajectories.

Cellular and nuclear membranes were reconstructed in 3D space taking advantage of specific labeling. For each membrane, a mask was produced using Otsu's method and improved with a sequence of morphological operators (namely image close, dilation and

erosion, small objects removal). The orientation axis for the membranes were calculated using principal components analysis (PCA) of a large sample of membrane surface points. This method using PCA was found to be more robust that ellipsoid fitting to the membrane surface (followed by extraction of the axis vectors). From the centrosomes locations and nuclear membrane reconstruction, it was possible to calculate the angle between the centrosomes axis and the nucleus major axis.

Quantification of nuclear membrane surface fluctuation was performed in 2D using a single slice with a pixel size of 0.102μm. The coordinates of the pixels in the membrane contour were extracted for each frame by first reducing noise with a median filter (neighborhood of 3×3 pixels) followed by object segmentation. The segmentation used a statistical threshold (median + standard deviation), and was improved with small objects removal and closure morphological operations. Importantly, the (Euclidean) coordinates of the nuclear membrane pixels were converted to polar coordinates. The reference center was defined as the centroid of the membrane contour obtained by the median intensity projection of all frames. The polar coordinates allowed the decomposition of the fluctuations normal to the nuclear contour (captured in the radial coordinate). The analysis was limited to 60° angular apertures centered on the membranes main axis. Different methods were designed to explore, analyze and visualize the radial components of the membrane contour. In these methods, the membrane radial fluctuations were characterized using statistics such as maximal amplitudes or standard deviation of the radial component.

Preparation of micropatterned hydrogels with nanobeads

Firstly, 32mm coverslips are plasma cleaned for 30 sec and then incubated with a drop of PLL-PEG 0.1 mg/mL in HEPES 10 mM ph7.4 for 30 min at RT as described previously (Vignaud et al., 2014). Coverslips are then put upright to let the excess PLL-PEG run off and placed on a line or circle shape quartz photomask (Toppan) on a 3μl drop of MilliQ water. The coverslips on the photomask are then exposed to deep-UV for 5 min. Then, coverslips are detached from the photomask and incubated with 20μg/ml fibronectin (Sigma) and 20μg/ml Alexa546-conjugated fibrinogen (Invitrogen) in PBS for 30 min at RT. To prepare the gels, a 42μl drop of 40KPa mix of Polyacrylamide (Sigma) and bisacrylamide containing 0,1μl carboxylate-modified polystyrene fluorescent beads (Invitrogen) is placed onto the fibronectin coated coverslips and then covered with a second coverslip, pretreated with Bind-silane solution (100% ethanol solution containing 18.5μl Bind Silane; GE Healthcare Life Science) and 161μl 10% acetic acid (Sigma) for 5 min. Gels are polymerized for 30 min and finally the gel is retrieved with the silanized coverslip. Fibronectin proteins are trapped within the acrylamide mesh. Gels are stored in PBS at 4°C.

Traction force microscopy (TFM) imaging and analyses

For TFM live-cell imaging, line or circle-micropatterned coverslips are mounted in dedicated chambers and supplemented with L-15/10% FBS medium. Leica SP8 confocal microscope was used to acquire the images using a 40X objective (oil immersion, numerical aperture 1.3), with a confocal microscope (Leica TCS-SP8) and a temperature control chamber set at 37°C. Cells expressing alpha–tubulin-GFP and H2B-mcherry were acquired every 3 min. 488 nm and 533 nm lasers were used in sequential scanning

mode. All the laser parameters and imaging setups are controlled through the LAS X system. Cellular traction forces were calculated using a method previously described (Mandal et al., 2014). Briefly, at each time point, the image of the fluorescent beads embedded in the substrate was compared to a reference image corresponding to a relaxed substrate and taken after washing away the cells. After correcting for experimental drift, the displacement field was obtained by a two-step process consisting of cross-correlation on 9.6μm sub-images followed by particle tracking to improve the spatial resolution. The final displacement field was interpolated to a regular grid with 1.2μm spacing. Traction stress reconstruction was performed with the assumption that the substrate is a linear elastic half-space using Fourier transform traction cytometry (FTTC) and zeroth order regularization. The stress map was defined on the same 1.2μm-period grid. From this stress map and the cell mask, we checked that the out of equilibrium force is less than 10% of the sum of forces magnitude, as a quality criterion for all cells and time points. The contractile energy, which is the mechanical energy transferred from the cell to the substrate, was computed from the traction map by integrating the scalar product of the displacement and stress vectors over the cell surface. To determine the principal direction of contraction of each cell, we calculated and diagonalized the first moment tensor of the stress. The eigenvector corresponding to the larger eigenvalue gives the direction of the main force dipole. The degree of force polarization is obtained by comparing both eigenvalues. All the calculations are performed in Matlab (The MathWorks Inc., USA; R2018a).

EB3 comet tracking and analysis

For microtubule dynamics analysis, images of EB3-GFP were acquired as a single slice with a time lapse of 500ms. Raw unprocessed images were tracked automatically using the plusTipTracker software (Applegate et al., 2011). The following parameters were set in the program: search radius range 3-12 pixel; minimum sub-track length 3 frames; gap length 2-6 frames; maximum forward angle 30; maximum backward angle 10; fluctuation radius 2. For statistical analysis, the plusTipGroupAnalysis function was used to compare the dynamic parameters between groups. Dynamic parameters were obtained from multiple experiments.

Immunofluorescence

HeLa cells were fixed with 4% PFA in Cytoskeleton Buffer (274 mM NaCl, 2.2mM Na2HPO4, 10mM KCL, 0.8 mM KH2PO4, 4 mM EDTA, 4 mM MgCl2, 10 mM Pipes, 10 nM Glucose, pH 6.1) and subsequently permeabilized with 5% Triton X-100 (Sigma-Aldrich) in 1x PBS for 5 minutes. After three short washes in 10% Triton X-100 in 1x PBS for 5 min, the cells were blocked with 10% FBS in 10% Triton X-100 in 1x PBS for 30 min. All the primary antibodies were diluted in blocking solution and incubated for 1h at room temperature. After this incubation the cells were washed with 10% Triton X-100 in 1x PBS and incubated with the respectively secondary antibody during 1h at room temperature. The secondary antibodies were also diluted in blocking solution. DNA was stained with DAPI which was added to the secondary antibodies solution (1ug/ml Sigma-Aldrich). After the incubation with the secondary antibodies and DAPI the coverslips were washed with 10% Triton X-100 in 1x PBS and sealed on glass slides mounted with 20mM Tris pH8, 0.5 N-propyl gallate and 90% glycerol. The following primary antibodies were used: mouse anti- Lamin A+C (1:500 Abcam), rabbit anti- Lamin B1 (1:500 Abcam), rat

anti- alpha Tubulin (1:500 Bio-Rad). The antibodies Alexa Fluor 488, 568 and 647 (1:2000 Invitrogen) were used as secondary antibodies. Images were acquired using an AxioImager Z1 (63x, Plan oil differential interference contract objective lens, 1.4 NA; all from Carl Zeiss) which is coupled with a CCD camera (ORCA-R2; Hamamatsu Photonics) using the Zen software (Carl Zeiss).

Western Blotting

HeLa cell extracts were collected after trypsinization and centrifuge at 1200 rpm for 5 minutes. The pellet was resuspended in 1x PBS and centrifuge again, the cells were resuspended in 30-50μL of Lysis Buffer (NP-40, 20 nM HEPES/KOH pH 7.9 ; 1 mM EDTA pH 8; 1 mM EGTA; 150 mM NaCl; 0.5% NP40; 10% glycerol, 1:50 protease inhibitor; 1:100 Phenylmethylsulfonyl fluoride). The samples were then flash frozen in liquid nitrogen and kept on ice for 30 min. After centrifugation at 14000 rpm for 8 min at 4° C the supernatant was collected and protein concentration determined by the Bradford protein assay (Bio-Rad). The proteins were run on 7%/8%/10%/12%/15% SDS-PAGE (50μg per lane) and transferred, using the iBlot Gel Transfer Device (Thermo Scientific), to a nitrocellulose Hybond-C membrane. With exception to the experiment testing DHC depletion were the protein samples were transferred using a wet blot apparatus for 3h at 70V, with constant Amperage. Afterwards the membranes were blocked with 5% Milk in TBS with 0.1% Tween-20 (TBS-T) for 1h at room temperature. The primary antibodies used were: mouse anti- Nde1 (1:500 Abnova), mouse anti- Lamin A+C (1:500 Abcam), mouse anti- LaminA (1:100 VWR), rabbit anti- ARPC4 (1:500 Bionova Cientifica), rabbit anti- BICD2 (1:500 Atlas Antibodies), rabbit anti- DYNC1H1 (1:500 Thermo Fisher), rat anti-Alpha Tubulin (1:1000 Bio-Rad), rabbit anti-Vinculin (1:3000 Thermo Fisher) and all of the primary antibodies were incubated over night at 4°C with shaking. After three washed in TBS-T the membranes were incubated with the secondary antibody for 1h at room temperature. The secondary antibodies used were anti-mouse-HRP and anti-rabbit-HRP used 1:5000. After several washes with TBS-T the detection was performed with Clarity Western ECL Substrate (Bio-Rad).

Statistical analysis and data presentation

When data are represented as box-whisker plots, the box size represents 75% of the population and the line inside the box represents the median of the sample. The size of the bars (whiskers) represents the maximum (in the upper quartile) and the minimum (in the lower quartile) values. Statistical analysis for multiple group comparison was performed using a parametric one-way analysis of variance (ANOVA) when the samples had a normal distribution. When the sample did not have a normal distribution, multiple group comparison was done using a nonparametric ANOVA (Kruskal-Wallis). All pairwise multiple comparisons were subsequently analyzed using either post-hoc Student-Newman-Keuls (parametric) or Dunn's (nonparametric) tests. When comparing only two experimental groups, a parametric t test was used when the sample had a normal distribution, or a nonparametric Mann-Whitney test was used for samples without normal distribution. All statistical analyses were performed using SigmaStat 3.5 (Systat Software, Inc.).

Supplemental Information and Legends:

Supplementary Figure 1 - Effect of substrate coating on centrosome separation efficiency, related to Figure 1

(A) HeLa cells expressing H2B-GFP/alpha-tubulin-RFP were seeded either on FBN (n=59) or PLL (n=41) and imaged to determine whether they separated ("P pathway") or not ("PM pathway") their centrosomes during mitotic entry. (B) Correlation between pole-to-pole distance (in μm) and cell area at NEB (in μm^2) for cells seeded in FBN or PLL, taking into account their centrosome separation pathway. Cells with decreased area have lower pole-to-pole distances.

Supplementary Figure 2 - Representative output from custom-designed MATLAB computational tools, related to Figure 1

(A) Representative reconstruction of HeLa cell showing cell membrane (red), nucleus (green) and centrosome vector (blue). (B) Representative reconstruction of centrosomes vector (blue arrows), nuclear major (large green arrows) and minor (small green arrows) axes, and cellular major (large red arrows) and minor (small red arrows) axes. Each set of arrows corresponds to a time-point extracted from a live-cell imaging movie. (C) Reconstruction of centrosomes trajectories in 4D. (D) Pole-to-pole distances over time. (E) Representation of the centrosomes orientation vector relative to the underlying micropattern. Red corresponds to theta (variations in xy) and blue corresponds to phi (variations in z). (F) Representation of the variation in cell membrane eccentricity over time.

Supplementary Figure 3 - Centrosomes deviate from the long axis of the micropattern as cells round up.

Correlation between the average theta values (red; corresponding to centrosomes xy orientation), average phi values (blue; corresponding to centrosomes z orientation) and cell membrane eccentricity (black) for cells seeded on line micropatterns (n=30). This correlation was done using the average values plotted in graphs 1B (theta and phi) and 1C (eccentricity). The long axis of the micropattern was oriented horizontally and defined as a reference point, corresponding to a value of zero for theta and phi. Red line corresponds to NEB. Dashed black line highlights first event of cell rounding, which correlates with increases in theta and phi.

Supplementary Figure 4 - Variation in cell membrane eccentricity and centrosome separation for different micropatterns, related to Figure 2

Cell membrane eccentricity for cells seeded on large circles (A; 700μm^2; n=32), small circles (B; 80μm^2; n=16) or rectangles (C; 500μm^2; n=36). Individual dots correspond to a specific time-point extracted from reconstructed cell membranes. Lines represent average values and error bars represent standard deviation. (D) Quantification of centrosome separation behavior for cells seeded on different micropatterns.

Supplementary Figure 5 - TFM analysis of cells seeded on circle micropatterns, related to Figure 3

(A) Selected frames from representative time-lapse movie of a HeLa cell expressing H2B-GFP/alpha-tubulin-RFP seeded on a PAA hydrogel with a circle micropattern (left panel). Right panel corresponds to brightfield (BF) image overlaid with the corresponding traction force map (red arrows). Red line corresponds to the axis of symmetry. Green line corresponds to the main direction of the force dipole. Magenta line corresponds to the secondary direction of the force dipole. (B) Traction force orientation, showing high

variability of force axes, when the cell axis of symmetry is taken as a reference point. (C) Correlation between centrosome orientation axis (theta; red) and traction axis (blue). (D) Correlation between contractile energy (EC; blue) and cell area (red) for cells seeded on circles (n=17).

Supplementary Figure 6 - Modifying cytoskeletal tension affects cell rounding and centrosome movement, related to Figure 3

(A) Quantification of theta (red) and phi (blue) for mock transfected (n=36), Rap1* (n=30), DMSO (n=39) and Y-27632 (n=35) cells. Individual dots correspond to a specific time-point extracted from reconstructed centrosome trajectories. Lines represent average values, which were used to plot panels in Figure 3G. (B) Cell membrane eccentricity for mock transfected, Rap1*, DMSO and Y-27632 cells. Individual dots correspond to a specific time-point extracted from reconstructed cell membranes. Lines represent average values and error bars represent standard deviation. Average values were used to plot panels in Figure 3G. (C) Selected frames from representative movie showing mitotic entry of a HeLa cell expressing EB3-GFP/Lifeact-mCherry treated with PTx (n=31). Time-lapse is 20 sec. Scale bar, 10μm. (D) Quantification of theta (red) and phi (blue) for cells treated with PTx. Individual dots correspond to a specific time-point extracted from reconstructed centrosome trajectories. Lines represent average values, which were used to plot panels in Figure 3J (E) Cell membrane eccentricity for cells treated with PTx. Individual dots correspond to a specific time-point extracted from reconstructed cell membranes. Lines represent average values and error bars represent standard deviation. Average values were used to plot panel 3K.

Supplementary Figure 7 - Eg5 is required for early, but not late, centrosome separation. Related to Figure 4

(A) Polar plot quantifying centrosome positioning (red circles) relative to the short nuclear (blue ellipse) at NEB for cells treated with STLC when centrosomes were already on opposite sides of the nucleus (Late stage; green ; n=12) or when centrosomes were still not completely separated (Early stage; red; n=30). (B) Pole-to-pole distance for cells treated with STLC in either the Early stage (red) or the Late stage (green) of centrosome separation. Note how pole-to-pole distance only decreases in Late stage cells when cell rounding begins (~600sec before NEB). Correlation between the average theta values (red; corresponding to centrosomes xy orientation), average phi values (blue; corresponding to centrosomes z orientation) and cell membrane eccentricity (black) for cells in early (C) or late (D) stage of centrosome separation. The long axis of the micropattern was oriented horizontally and defined as a reference point, corresponding to a value of zero for theta and phi.

Supplementary Figure 8 - Interfering with Arp2/3 activity affects centrosome movement and mitotic cell rounding, related to Figure 4

Correlation between theta (red; corresponding to centrosomes xy orientation) and phi (blue; corresponding to centrosomes z orientation) for cells treated with CK666 (A; n=41) or ARPC4 RNAi (C; n=34), seeded on line micropatterns. The long axis of the micropattern was oriented horizontally and defined as a reference point, corresponding to a value of zero for theta and phi. Individual dots correspond to a specific time-point extracted from reconstructed centrosome trajectories. Cell membrane eccentricity for cells treated with CK666 (B) or ARPC4 RNAi (D), seeded on line micropatterns. Individual dots correspond to a specific time-point extracted from reconstructed cell membranes. Lines represent average values and error bars represent standard

deviation. Average values for theta, phi and eccentricity in CK666-treated cells were used to plot graph in Fig. 4B. (E) Representative immunoblot to confirm ARPC4 depletion efficiency by RNAi.

Supplementary Figure 9 - Microtubule stabilization impairs centrosome movement as cells prepare to enter mitosis, related to Figure 4

Cells treated with 20nM Taxol were filmed during mitotic entry. (A) Correlation between theta (red; corresponding to centrosomes xy orientation) and phi (blue; corresponding to centrosomes z orientation) for cells treated with Taxol seeded on line micropatterns (n=15). The long axis of the micropattern was oriented horizontally and defined as a reference point, corresponding to a value of zero for theta and phi. Individual dots correspond to a specific time-point extracted from reconstructed centrosome trajectories. (B) Cell membrane eccentricity for cells treated with Taxol, seeded on line micropatterns. Individual dots correspond to a specific time-point extracted from reconstructed cell membranes. Lines represent average values and error bars represent standard deviation. (C) Polar plot quantifying centrosome positioning (red circles) relative to the short nuclear (blue ellipse) at NEB for cells treated with Taxol. (D) Correlation between the average theta values (blue; corresponding to centrosomes xy orientation), average phi values (red; corresponding to centrosomes z orientation) and cell membrane eccentricity (black). Average values obtained from panels (A) and (B).

Supplementary Figure 10 - Interfering with Dynein on the nuclear envelope affects centrosome positioning at NEB, related to Figure 4

(A) Correlation between theta (red; corresponding to centrosomes xy orientation) and phi (blue; corresponding to centrosomes z orientation) for cells treated with NudE/NudEL RNAi seeded on line micropatterns (n=36). The long axis of the micropattern was oriented horizontally and defined as a reference point, corresponding to a value of zero for theta and phi. Individual dots correspond to a specific time-point extracted from reconstructed centrosome trajectories. (B) Cell membrane eccentricity for cells treated with NudE/NudEL RNAi, seeded on line micropatterns. Individual dots correspond to a specific time-point extracted from reconstructed cell membranes. Lines represent average values and error bars represent standard deviation. Average values for theta, phi and eccentricity were used to plot graphs in Figures 4I and J. Polar plot quantifying centrosome positioning (red circles) relative to the short nuclear (blue ellipse) at NEB for cells treated with DHC RNAi (C; n=31) or BicD2 RNAi (D; n=34). (E) Representative immunoblots to confirm depletion efficiency by RNAi of NudE/NudEL (E), DHC (F) and BicD2 (G).

Supplementary Figure 11 - Nucleo-cytoskeletal uncoupling does not prevent centrosome positioning on the short nuclear axis, related to Figure 5

(A) Selected frames from a representative time-lapse movie of a HeLa cell expressing EB3-GFP/Lifeact-mCherry and transfected with a KASH-GFP construct. Time-lapse is 20 sec. Scale bar, 10μm. (B) Polar plot quantifying centrosome positioning (red circles) relative to the short nuclear (blue ellipse) at NEB for cells expressing KASH-GFP seeded on line micropatterns (n=30). (C) Correlation between theta (red; corresponding to centrosomes xy orientation) and phi (blue; corresponding to centrosomes z orientation) for cells expressing KASH-GFP, seeded on line micropatterns (n=36). The long axis of the micropattern was oriented horizontally and defined as a reference point, corresponding to a value of zero for theta and phi. Individual dots correspond to a specific time-point extracted from reconstructed centrosome trajectories. (D) Cell membrane

eccentricity for cells expressing KASH-GFP, seeded on line micropatterns. Individual dots correspond to a specific time-point extracted from reconstructed cell membranes. Lines represent average values and error bars represent standard deviation.

Supplementary Figure 12 - Characterization of nuclear envelope fluctuations in interphase and prophase, related to Figure 5

HeLa cells expressing POM121-3xGFP/H2B-mCherry and SiR-tubulin were imaged with a time-lapse of 100msec to measure nuclear envelope fluctuations. (A) Quantification of interphase nuclear membrane fluctuation amplitude for the long and short axes in controls, ICRF-193, Lamin A RNAi and Noco (*** $p<0.001$; ** $p<0.01$). (B) Quantification of interphase nuclear fluctuation standard deviation from the median for controls (n=39), ICRF-193 (n=16), Lamin A RNAi (n=25) and Nocodazole (Noc; n=32) (***$p<0.001$; ** $p<0.01$). (C) Quantification of nuclear membrane fluctuation amplitude for the long and short axes in control cells (*** $p<0.001$). (D) Quantification of prophase nuclear membrane fluctuation amplitude for the long and short axes in controls, ICRF-193, Lamin A RNAi and Noco (*** $p<0.001$; ** $p<0.01$; n.s. - not significant). (E) Representative immunoblot to confirm depletion efficiency by RNAi of Lamin A in HeLa cells expressing POM121-3xGFP/H2B-mCherry.

Supplementary Figure 13 - Mitotic entry in cells treated with ICRF-193 and Lamin A RNAi, related to Figure 5

Selected frames from a representative time-lapse movie of a HeLa cell expressing EB3-GFP/Lifeact-mCherry treated with ICRF-193 (A) or Lamin A RNAi (D). Time-lapse is 20 sec. Scale bar, 10μm. Correlation between theta (red; corresponding to centrosomes xy orientation) and phi (blue; corresponding to centrosomes z orientation) for cells treated with ICRF-193 (B) or Lamin A RNAi (E), seeded on line micropatterns. The long axis of the micropattern was oriented horizontally and defined as a reference point, corresponding to a value of zero for theta and phi. Individual dots correspond to a specific time-point extracted from reconstructed centrosome trajectories. Solid lines correspond to average values. Cell membrane eccentricity for cells treated with ICRF-193 (C) or Lamin A RNAi (F), seeded on line micropatterns. Individual dots correspond to a specific time-point extracted from reconstructed cell membranes. Lines represent average values and error bars represent standard deviation. (G) Representative immunoblot to confirm Lamin A depletion efficiency by RNAi in HeLa cells expressing EB3-GFP/Lifeact-mCherry.

Supplementary Figure 14 - Immunofluorescence analysis of BicD2, Lamin A and Lamin B1, related to Figure 5

(A) Representative images of immunofluorescence analysis of BicD2 (Alexa488), Lamin B1 (Alexa594), alpha-tubulin (Alexa 647) and DAPI for controls, ICRF-193 and Noco. (B) Representative images of immunofluorescence analysis of Lamin A/C-C (Alexa488; green), Lamin B1 (Alexa 594; red), alpha-tubulin (Alexa 647; infrared) and DAPI (blue) for controls, Noco, DHC RNAi and ICRF-193. All images correspond to deconvoluted, maximal intensity projections. Scale bar, 10μm.

Supplementary Figure 15 - Detailed characterization of mitotic progression, related to Figure 6

(A) Timings from NEB to metaphase plate and from metaphase plate to anaphase onset, for cells seeded on FBN (n=35) or PLL (n=47), according to their centrosome separation status (*** $p<0.001$; n.s. - not significant). (B) Quantification of the type of missegregation

events for cells seeded on FBN or PLL. (C) Timings from NEB to metaphase plate and from metaphase plate to anaphase onset, for cells seeded on FBN and treated with DMSO (n=40) or CK666 (n=37) (** $p<0.01$; n.s. - not significant). (D) Quantification of the type of missegregation events for cells seeded on FBN treated with DMSO or CK666.

Supplementary Video 1 - HeLa cell expressing EB3-GFP/Lifeact-mCherry seeded on a line micropattern during mitotic entry, related to Figure 1

Supplementary Video 2 - HeLa cell expressing EB3-GFP/Lifeact-mCherry seeded on a large circle micropattern during mitotic entry, related to Figure 2

Supplementary Video 3 - HeLa cell expressing EB3-GFP/Lifeact-mCherry seeded on a line micropattern treated with Y-27632, related to Figure 3

Supplementary Video 4 - HeLa cell expressing H2B-GFP/tubulin-RFP treated with Nde/Ndel RNAi, seeded on a line micropattern, related to Figure 4

Supplementary Video 5 - HeLa cell expressing DHC-GFP, related to Figure 5

Supplementary Video 6 - HeLa cell expressing H2B-GFP/tubulin-RFP seeded on FBN, related to Figure 6.

Supplementary Video 7 - HeLa cell expressing H2B-GFP/tubulin-RFP seeded on PLL, showing a missegregation event, related to Figure 6

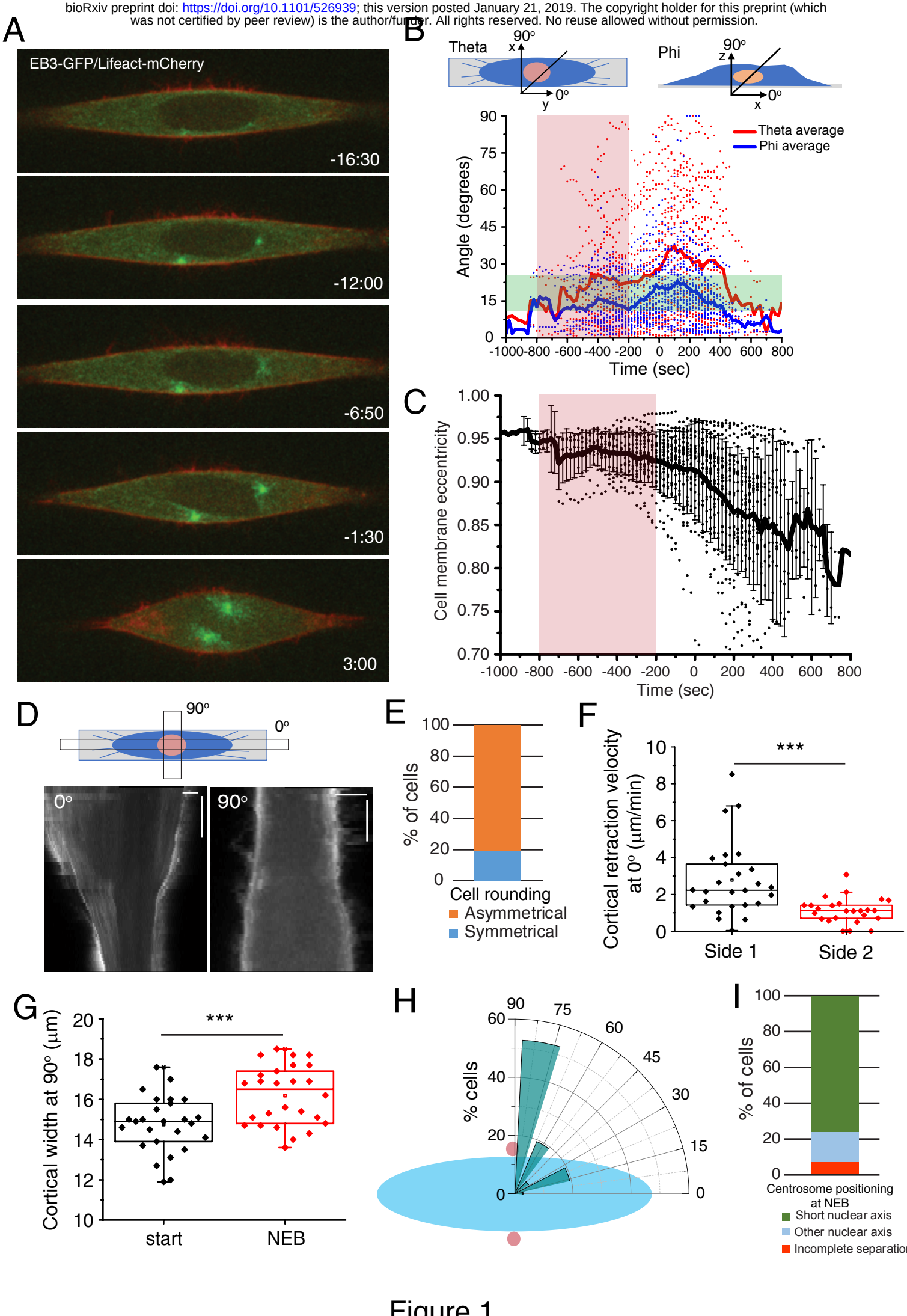

Figure 1

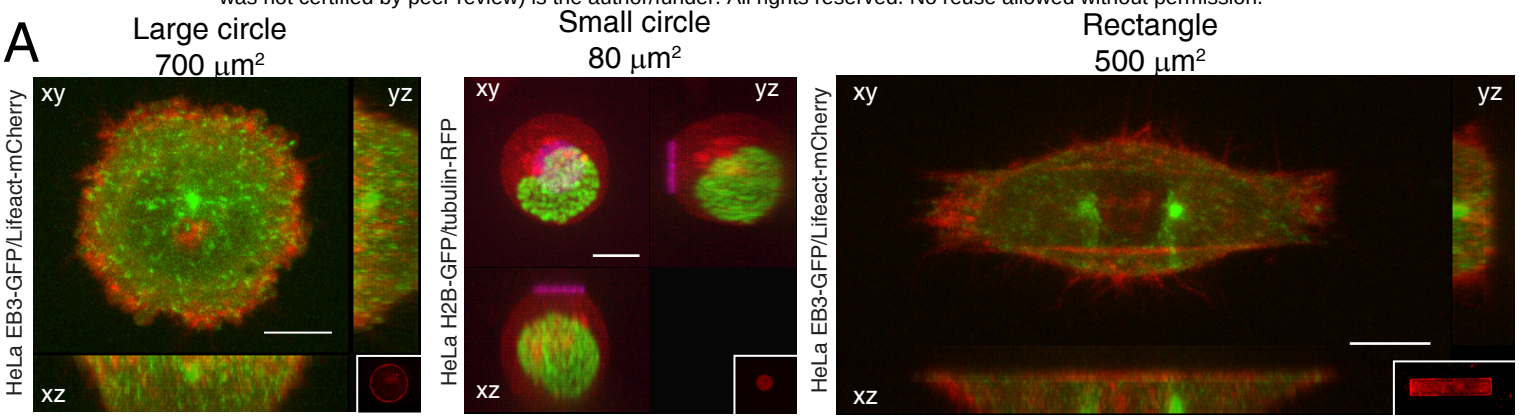

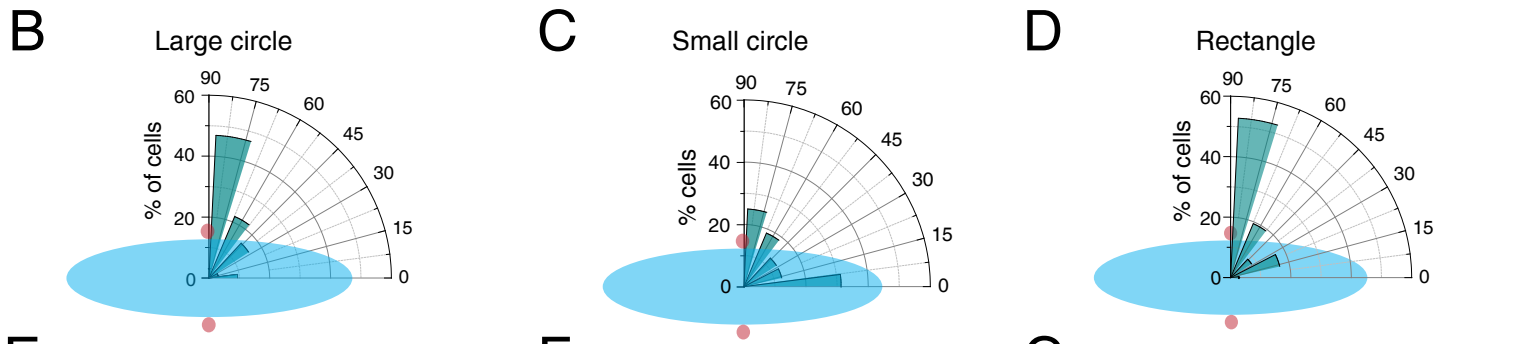

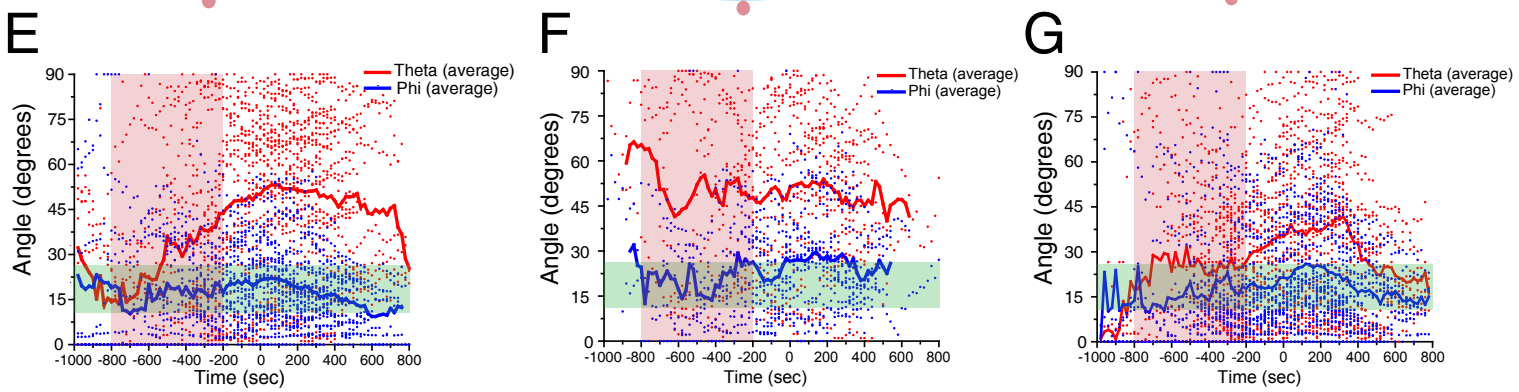

Figure 2

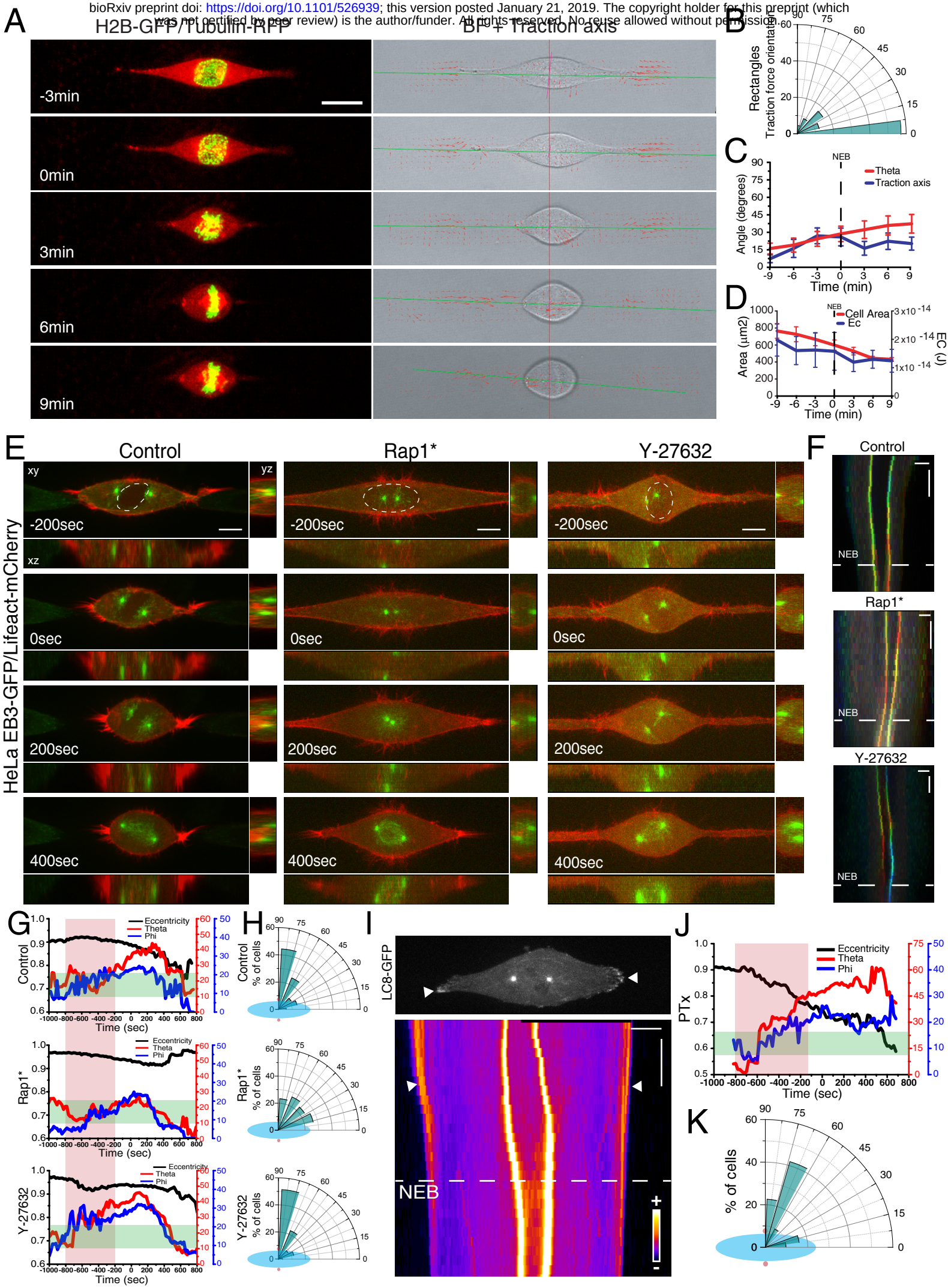

Figure 3

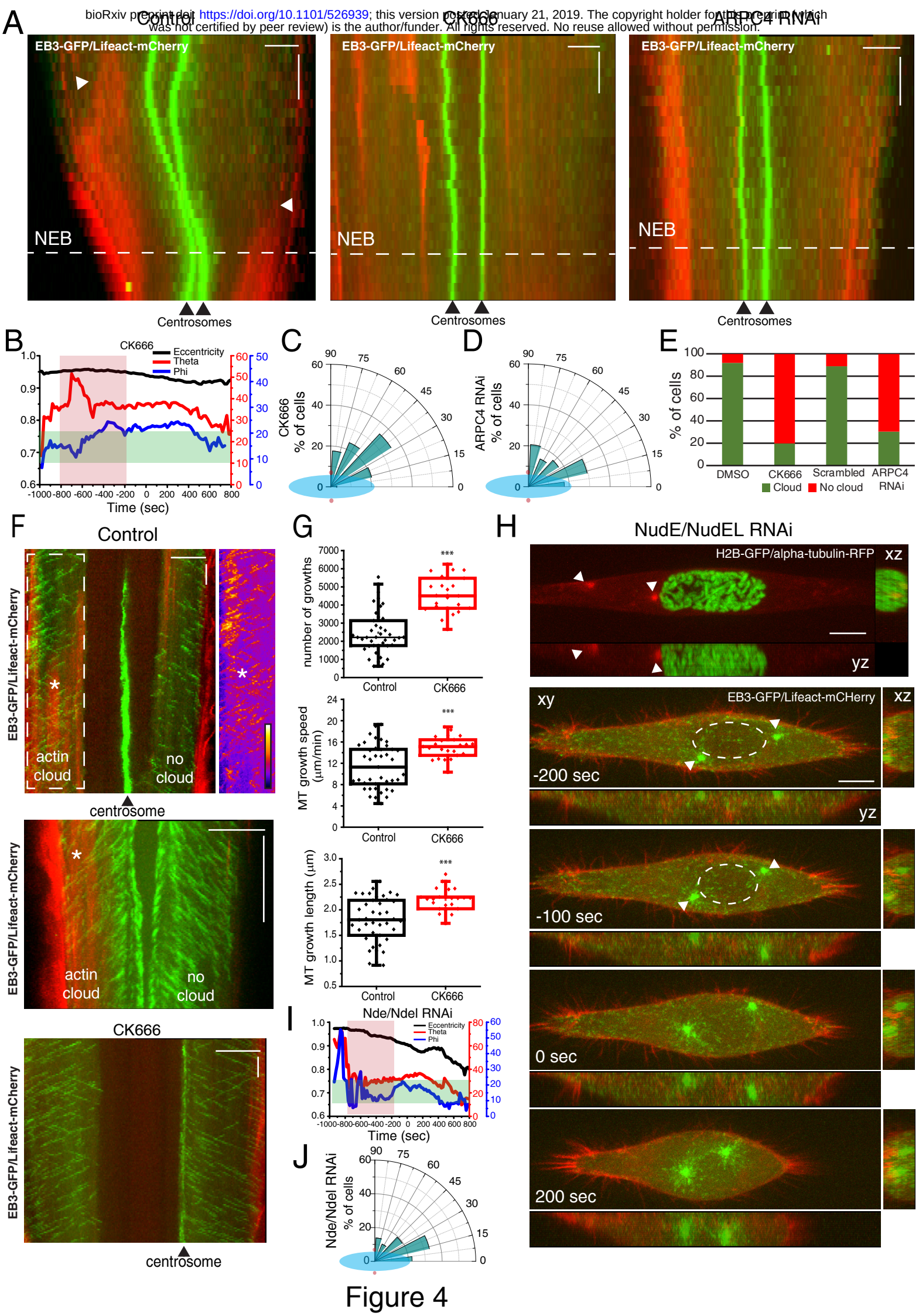

Figure 4

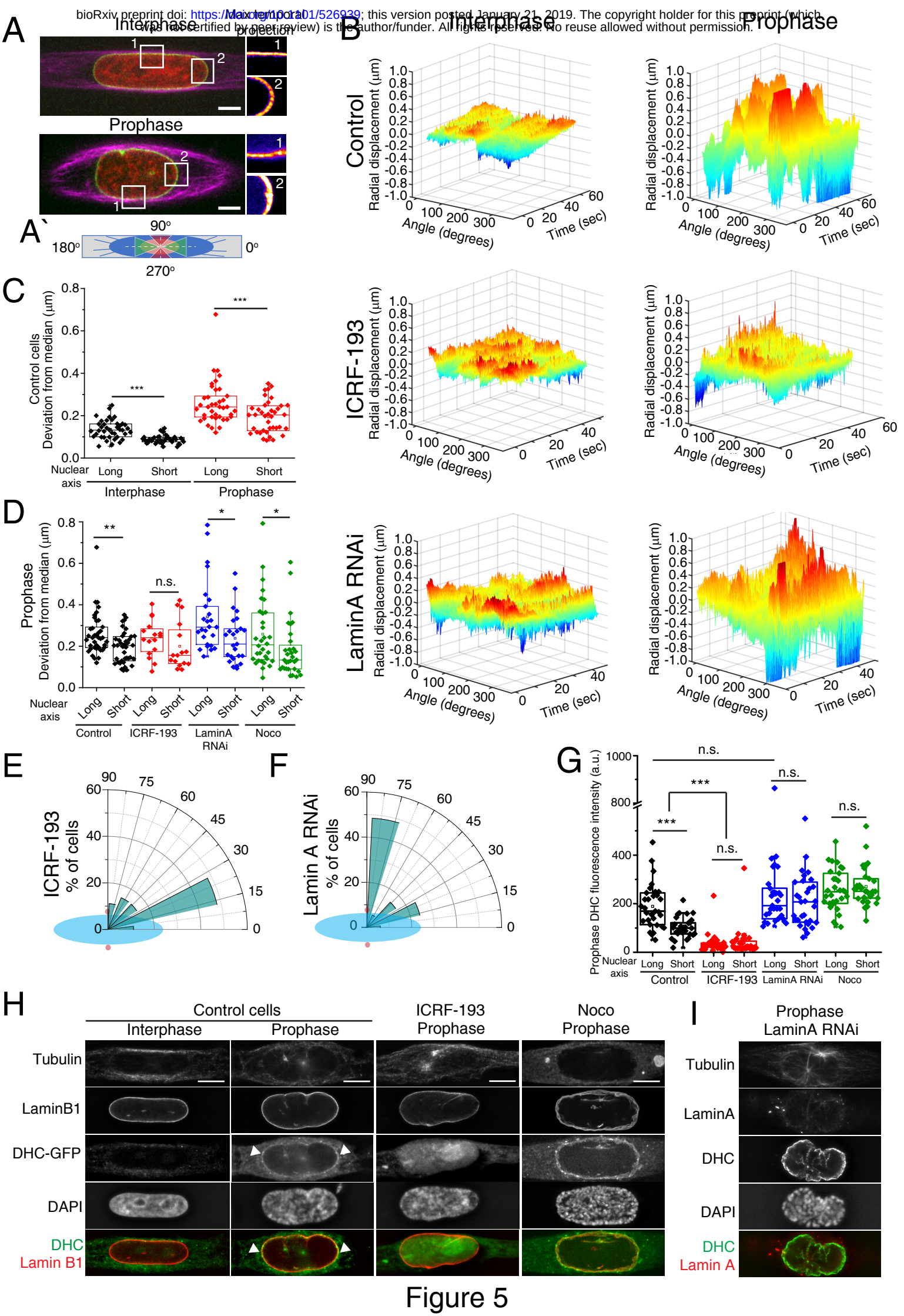

Figure 5

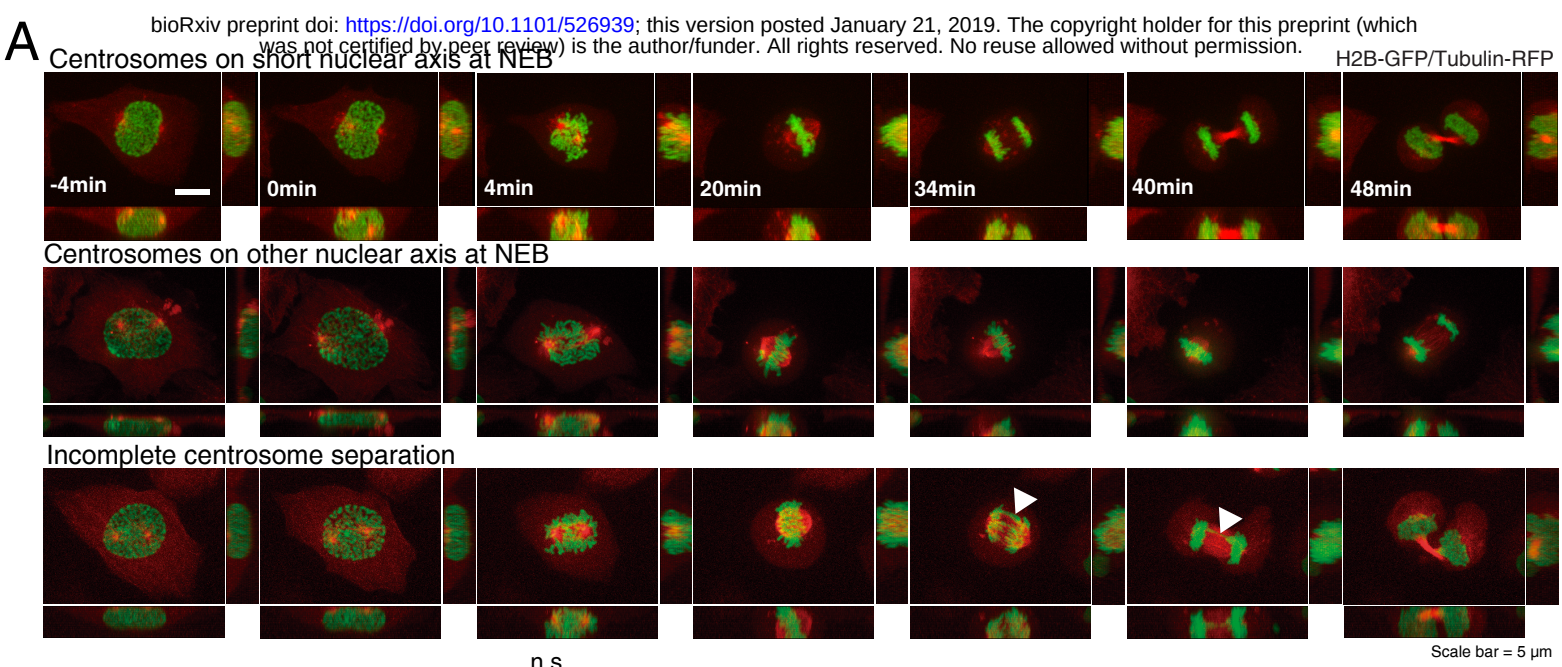

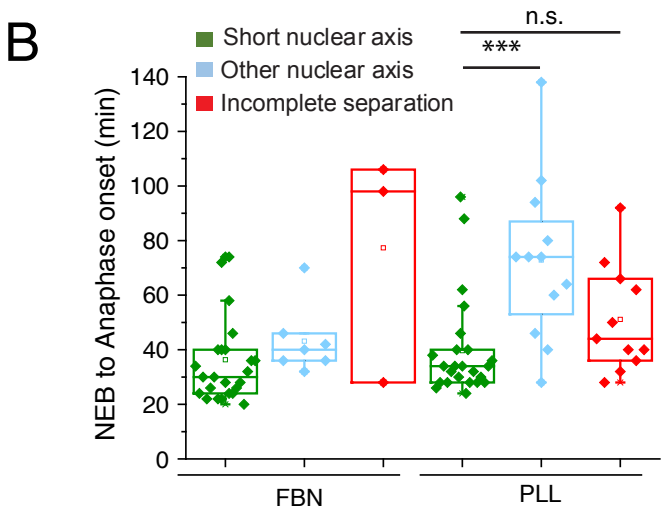

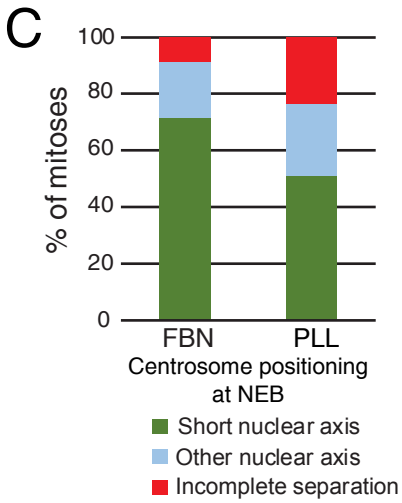

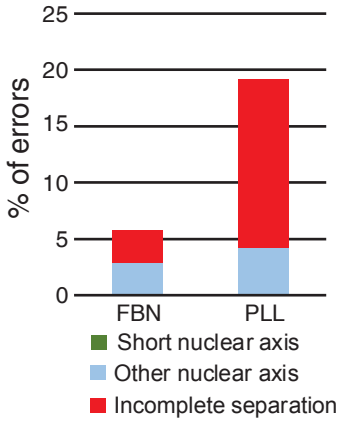

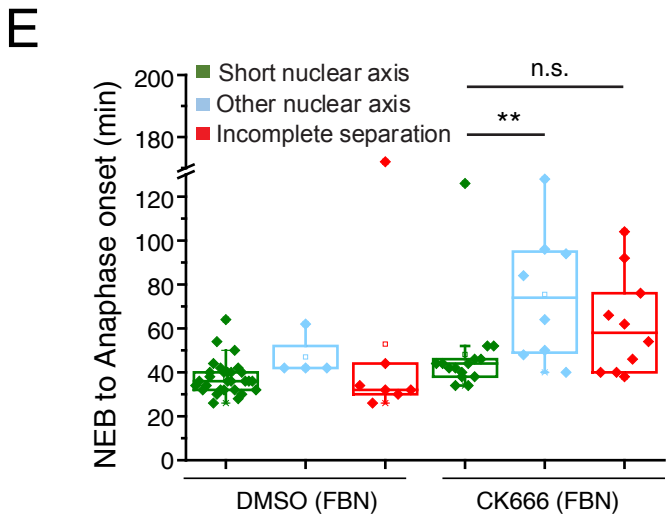

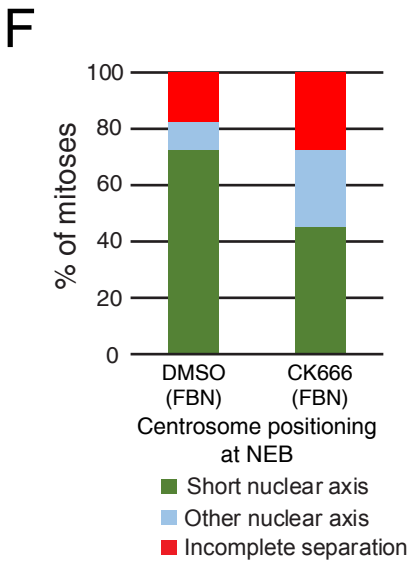

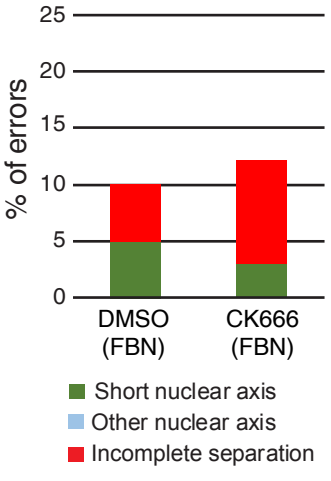

Figure 6